J. Fluid Mech. (2006), *vol.* 564, *pp.* 227–266.
doi:10.1017/S0022112006001479 Printed in the United Kingdom

A boundary-integral study of a drop squeezing through interparticle constrictions

By ALEXANDER Z. ZINCHENKO AND ROBERT H. DAVIS

Department of Chemical and Biological Engineering, University of Colorado, Boulder, CO 80309-0424, USA
zinchenk@spot.colorado.edu; robert.davis@colorado.edu

(Received 27 September 2005 and in revised form 6 March 2006)

A three-dimensional boundary-integral algorithm is developed to study the squeezing of a deformable drop through a tight constriction formed by several solid particles rigidly held in space. The drop is freely suspended and driven by a flow that is uniform away from the solid obstacles. Particular emphasis is on the trapping mechanism and flow conditions close to critical, when the drop squeezes with high resistance. The problem is a close prototype of drop–solid interactions for emulsion flow through a granular material; such interactions are much more lubrication-sensitive than drop–drop interactions and require advanced numerical tools to succeed. The algorithm is based on the Hebeker representation for the solid–particle contribution, leading to a well-behaved system of second-kind integral equations, combined with novel regularization techniques for singular and near-singular boundary integrals; high-order near-singularity subtraction for the solid-to-drop double-layer contribution is the most crucial element. Simulations are performed for drop squeezing between (i) two close spheres, (ii) two parallel spheroidal disks, and (iii) three close spheres forming an equilateral triangle (including the case of close solid–solid contact). The drop non-deformed diameter is from two to several times larger than the inner constriction diameter and, in some simulations, the drop decelerates 10^3–10^4 times in the throat before being able to pass through. The effects of the constriction type, capillary number, and viscosity ratio on the drop velocity in the throat, exit time, and drop–solid spacing (of the order of 1% of the particle size) are explored in detail; critical capillary numbers (below which trapping occurs) are accurately determined. Even for a substantially supercritical capillary number, the drop has to nearly coat solid particles to be able to pass through a tight constriction. The ability of the algorithm to simulate both supercritical and subcritical conditions (when the drop is trapped, with a small but non-zero drop–solid spacing) is vital for future applications to large-scale simulations of emulsion flow through granular media.

1. Introduction

Emulsion flow through a granular material is a problem of fundamental importance relevant to many industrial applications (oil filtration through underground reservoirs, flow through fixed-bed catalytic reactors, etc.). Among fundamental issues are the pressure gradient–flow rate relationship and determining the conditions when the dispersed phase flow rate effectively vanishes owing to emulsion drop blockage in the pore throats between granular particles. The mechanics of emulsion flow through a granular material is very complex because of the intricate geometry of the pore space. For

flows strong enough to overcome drop blockage in the pores by capillary forces, the possibility of drop breakup is another complication. If the emulsion drops were small compared to the typical pore diameter, a continuum model for an emulsion with some effective properties would be appropriate; unfortunately, in many cases of practical interest, emulsion drops are not so small (Kokal, Maini & Woo 1992), and more complex microstructural modelling must be developed instead.

To simplify the problem, many workers studied the axisymmetrical pressure-driven creeping motion of a single drop through constricted capillary tubes as a prototype model for emulsion flow through a porous material. Olbricht & Leal (1983) and Hemmat & Borhan (1996) performed experiments to measure pressure drop-flow rate characteristics and elucidate conditions for droplet breakup. Martinez & Udell (1988) analysed the problem by boundary-integral simulations, but did not observe snap-off. Tsai & Miksis (1994), in their boundary-integral study, observed breakup, with a sizeable minor fragment, even for drop-to-medium viscosity ratio of $\lambda = 0.001$. In addition to these and other studies (Leyrat-Maurin & Barthès-Biesel 1994; Borhan & Hemmat 1997; Quèguiner & Barthès-Biesel 1997) on axisymmetrical motion through constrictions, there is a rich body of literature on single drop motion through straight capillary tubes not discussed here (see Olbricht 1996 for a comprehensive review on early work). A distinctive feature of a constricted capillary tube, which makes this model more relevant to emulsion flow through granular materials, is the existence of the critical forcing (for a sufficiently large drop), below which the drop cannot pass the constriction and is trapped instead at the pore throat, with very small drop–wall spacing. The trapping mechanism, however, has been studied much less than drop breakup in capillaries, because of numerical difficulties. The work of Leyrat-Maurin & Barthès-Biesel (1994), on a related problem of a deformable capsule in a hyperbolic constriction, was the first attempt to address this important issue, but, unfortunately, their calculations suffered from the inability of the algorithm to handle small drop–wall spacings inherent in the trapping phenomenon. To our knowledge, this restrictive feature is common for all previous axisymmetrical calculations for drop/capsule motion through constricted tubes based on solving the first-kind integral equation for wall tractions. A recent preconditioned three-dimensional version for a capsule in a straight capillary (Pozrikidis 2005), which is also based on solving the first-kind integral equation for tractions, has the same limitation. Instead of a boundary-integral method, Graham & Higdon (2000*a*, *b*) used a finite-element approach and fine adaptive domain meshing to study axisymmetrical drop squeezing through a tight constriction, with the drop non-deformed radius being up to twice as large as the throat radius. Although the thin lubrication layers complicate computations, Graham & Higdon were able to address the near-contact drop–wall interaction and estimate the critical forcing level necessary for squeezing. Moreover, the study of Graham & Higdon (2000*a*, *b*) is for non-zero Reynolds numbers, Re, and includes the effect of oscillatory forcing on drop squeezing. One of the conclusions from their work is that inertial effects do not manifest themselves until the property number Re/Ca reaches $O(10^2)$; presumably, this conclusion can stimulate further work in the creeping-flow aproximation, since the microscale Reynolds number for emulsion flow through a granular material is often small.

In a different approach, a porous material skeleton was modelled as a random dilute bed of spheres or parallel fibres. Mosler & Shaqfeh (1997) replaced the effect of bed particles/fibres on a droplet by an effective stochastic Gaussian field derived from theory; perturbation solutions for small capillary numbers were used to predict the onset of drop breakup. Patel *et al.* (2003) used detailed boundary-integral solutions

for a single drop in an effective field around an individual fibre to include near-field effects and simulate large deformations and breakup. Their approach is similar to that for drop breakup in turbulent flows (Cristini *et al.* 2003); the use of the free-space Green function (instead of the Green function for the domain exterior to the fibre) was justified for dilute beds, when the average pore size is large compared to the drop dimensions. Both 'graze' and 'hairpin' modes of breakup were simulated by Patel *et al.* (2003), in qualitative agreement with their experiments.

Although these studies have provided substantial insight into the drop motion through confined geometries, it is recognized (Olbricht 1996) that more realistic models are required to fully understand and predict emulsion flow through granular materials. For example, drop trapping in three-dimensional interparticle constrictions is qualitatively different from pore plugging in tubes; there are many paths available for flow in a granular material, while there is only one path in the tube flow (Olbricht 1996). Obviously, a complete model for a granular material would be a random arrangement of globular particles (e.g. spheres or spheroids) in mechanical equilibrium (random 'loose' or 'close' packings; e.g. Zinchenko 1994, 1998), or, at least, a very dense unconsolidated packing. Such a model can be accurately prepared in a laboratory, with almost full control of microstructural parameters. In principle, a problem of creeping multidrop motion through a periodic box containing a large number of fixed solid inclusions can be formulated, and the pressure gradient–flow rate relationship can be rigorously established by long-time simulations, after adequate averaging.

As the first step towards the solution of this well-defined, but challenging simulation problem, we study here the prototype problem of flow-induced squeezing of a single deformable drop through a tight three-dimensional constriction formed by several solid particles rigidly held in unbounded space, with particular emphasis on the trapping mechanism and flow conditions close to critical. Under such conditions, the drop squeezes with maximum resistance (and very small drop–solid clearance), which makes this range particularly interesting to explore. The study of this problem not only allows us to clarify the salient features of emulsion squeezing through realistic granular materials, but also to develop and test numerical tools which could be combined in future work with efficient multipole acceleration techniques (Zinchenko & Davis 2000, 2002, 2003) for large-scale simulations. Compared to drop–drop interactions at finite deformations (e.g. Loewenberg & Hinch 1996, 1997; Zinchenko, Rother & Davis 1997, 1999; Bazhlekov, Anderson & Meijer 2004; Zinchenko & Davis 2004), the solution for drop–particle interactions is much more lubrication-sensitive, and has required advanced numerical techniques to succeed. The boundary-integral formulation is discussed in § 2. We start from Hebeker's (1986) representation for solid–particle contributions (as a proportional combination of a single- and double-layer potentials) to arrive at a system of well-behaved second-kind integral equations for the interfacial velocity on the drop surface and the Hebeker density on solid surfaces. Although Hebeker (1986) originally developed his approach for a single solid particle in a flow, the idea is also fruitful in the present problem, allowing for robust solutions both in the supercritical and subcritical range (when the drop is trapped); this feature could not be achieved with other boundary-integral formulations. It must be stressed that the approach based on the first-kind integral equation for tractions on the solid boundaries, which was so widely used in axisymmetrical tube flow simulations, is unsuitable in the present, more demanding three-dimensional problem owing to difficulties with close-contact interactions (as discussed in detail in § 4). Even more important for the present problem is the use of special desingularization techniques,

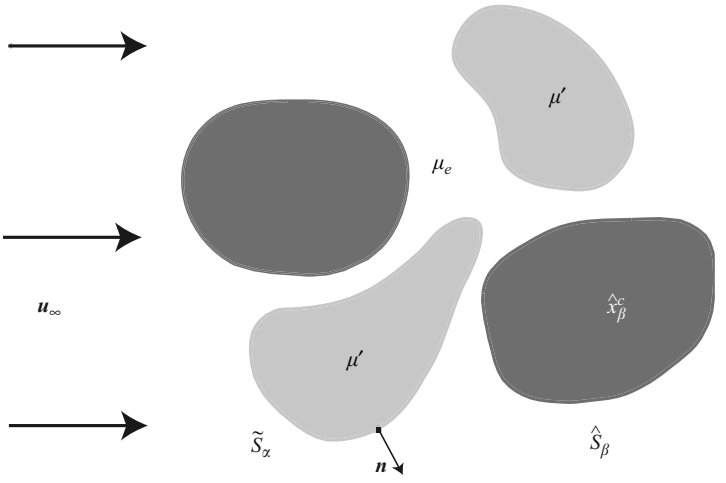

FIGURE 1. Sketch of the interaction of deformable drops (light shading) with solid particles (dark shading), not to scale.

especially novel high-order near-singularity subtraction in the solid–drop double-layer contribution, to handle close-contact drop–solid interactions. These techniques, along with other aspects of the algorithm, are described in § 3. In § 4, we give the results of numerical simulations for drop squeezing through a two-sphere and two-disk constriction, and between three close spheres forming an equilateral triangle (including the case of close contact). The effects of the constriction type, capillary number and viscosity ratio on the drop velocity in the throat, exit time and the drop–solid spacing are explored in detail; critical capillary numbers (for squeezing to occur) are accurately determined. Calculations are performed in a challenging range of parameter values, with the initial (non-deformed) drop diameter much larger than the inner constriction diameter and conditions not far from critical; in some simulations, the drop decelerates up to 10^3–10^4 times in the constriction, but it is still able to pass through. The trapped steady states (with small but non-zero drop–solid spacing) found for subcritical conditions appear to have some qualitative similarity to the stationary axisymmetrical solutions of Nemer (2003) and Nemer *et al.* (2004) for a drop near a plane wall and for two drops pressed together by a compressional flow, although the present problem is very different. The ability of our three-dimensional algorithm to maintain these trapped states virtually indefinitely, without a numerical crash, is a highly non-trivial feature (which could not be achieved without combining the Hebeker representation with new desingularizations) and is very important for the success of future large-scale simulations, as discussed in §§ 4–5. The Appendices contain some essential analytical and numerical details of our method.

2. Boundary-integral formulation

Consider a finite number $\widetilde{N}$ of three-dimensional deformable drops with surfaces $\widetilde{S}_1, \ldots, \widetilde{S}_{\widetilde{N}}$ freely suspended in a Stokes flow moving past a group of $\widehat{N}$ solid particles (figure 1). The particles are assumed to be rigidly held in space, with no-slip boundary conditions $\boldsymbol{u} = 0$ for the fluid velocity $\boldsymbol{u}$ on particle surfaces $\widehat{S}_1, \widehat{S}_2, \ldots, \widehat{S}_{\widehat{N}}$. The drops are free from surfactants, and they have density ρ matching that of the surrounding fluid, and a constant surface tension, σ. The fluids inside and outside the drops are Newtonian, with viscosities μ' and μ_e, respectively (figure 1). The flow at infinity,

$\boldsymbol{u}_\infty(\boldsymbol{y})$, is arbitrary in the formulation and solution method, but we will consider a uniform flow as a definite case in the calculations of § 4.

For numerical simulations, it would be easier to allow solid particles to move and rotate in this model formulation. However, such freedom of motion would significantly affect the mechanism of drop squeezing between solid particles and would not be relevant to future simulations of emulsion flow through a fixed-bed granular material, where solid particles form a rigidly held skeleton. On the other hand, with no-slip boundary conditions $\boldsymbol{u}=0$, this small-scale problem serves as a prototype for future, much more complex multidrop–multiparticle simulations to study salient features of the squeezing process and test the robustness of boundary-integral techniques for such simulations.

To derive a well-behaved system of Fredholm second-kind integral equations for this problem, we combine the ideas previously used for solitary drops (Rallison & Acrivos 1978) and single solid particles (Hebeker 1986). For a point $\boldsymbol{y}$ outside the drops and solid particles, Green's theorem applied to the Stokes flow $\Delta\boldsymbol{u}(\boldsymbol{y})=\boldsymbol{u}(\boldsymbol{y})-\boldsymbol{u}_\infty(\boldsymbol{y})$ gives

$$\Delta\boldsymbol{u}(\boldsymbol{y})=\sum_{\beta=1}^{\tilde{N}}\int_{\tilde{S}_\beta}\left[\frac{1}{\mu_e}\boldsymbol{G}(\boldsymbol{r})\cdot\Delta\boldsymbol{T}_n^e(\boldsymbol{x})-\Delta\boldsymbol{u}^e(\boldsymbol{x})\cdot\boldsymbol{\tau}(\boldsymbol{r})\cdot\boldsymbol{n}(\boldsymbol{x})\right]\mathrm{d}S_{\boldsymbol{x}}$$
$$+\sum_{\beta=1}^{\hat{N}}\int_{\hat{S}_\beta}\left[\frac{1}{\mu_e}\boldsymbol{G}(\boldsymbol{r})\cdot\Delta\boldsymbol{T}_n^e(\boldsymbol{x})-\Delta\boldsymbol{u}^e(\boldsymbol{x})\cdot\boldsymbol{\tau}(\boldsymbol{r})\cdot\boldsymbol{n}(\boldsymbol{x})\right]\mathrm{d}S_{\boldsymbol{x}},\quad(2.1)$$

where $\boldsymbol{r}=\boldsymbol{x}-\boldsymbol{y}$, $\Delta\boldsymbol{T}_n=(\boldsymbol{T}-\boldsymbol{T}_\infty)\cdot\boldsymbol{n}$, with $\boldsymbol{T}$ and $\boldsymbol{T}_\infty$ being the stress tensors for the flow fields $\boldsymbol{u}$ and $\boldsymbol{u}_\infty$, respectively, and $\boldsymbol{n}(\boldsymbol{x})$ the outward unit normal at $\boldsymbol{x}\in\tilde{S}_\beta$ or $\boldsymbol{x}\in\hat{S}_\beta$ (figure 1). Finally $\boldsymbol{G}(\boldsymbol{r})$ and $\boldsymbol{\tau}(\boldsymbol{r})$ are the free-space Green tensor and the corresponding fundamental stresslet:

$$\boldsymbol{G}(\boldsymbol{r})=-\frac{1}{8\pi}\left[\frac{\boldsymbol{I}}{r}+\frac{\boldsymbol{rr}}{r^3}\right],\quad\boldsymbol{\tau}(\boldsymbol{r})=\frac{3}{4\pi}\frac{\boldsymbol{rrr}}{r^5}.\quad(2.2)$$

The index e marks the values related to the domain exterior to drop and particle surfaces. Green's theorem for the interior of each surface $\tilde{S}_\beta$, $\hat{S}_\beta$ allows us to replace $\Delta\boldsymbol{u}^e$ and $\Delta\boldsymbol{T}_n^e$ by $\boldsymbol{u}^e$ and $\boldsymbol{T}_n^e$, respectively, in (2.1). Besides, using Green's theorem for the interior flow with viscosity μ' inside each drop $\tilde{S}_\beta$ yields

$$0=\int_{\tilde{S}_\beta}\left[\frac{1}{\mu_e}\boldsymbol{G}(\boldsymbol{r})\cdot\boldsymbol{T}_n^{int}(\boldsymbol{x})-\lambda\boldsymbol{u}^{int}(\boldsymbol{x})\cdot\boldsymbol{\tau}(\boldsymbol{r})\cdot\boldsymbol{n}(\boldsymbol{x})\right]\mathrm{d}S_{\boldsymbol{x}},\quad(2.3)$$

where $\lambda=\mu'/\mu_e$ is the viscosity ratio, and the index *int* relates to the quantities inside a drop.

Combining (2.1) and (2.3), and using interfacial boundary conditions for the velocity ($\boldsymbol{u}^e=\boldsymbol{u}^{int}$) and stress on drop surfaces gives a representation for the flow velocity in the domain exterior to the drops and solid particles

$$\boldsymbol{u}(\boldsymbol{y})=\boldsymbol{F}(\boldsymbol{y})+(\lambda-1)\sum_{\beta=1}^{\tilde{N}}\int_{\tilde{S}_\beta}\boldsymbol{u}(\boldsymbol{x})\cdot\boldsymbol{\tau}(\boldsymbol{r})\cdot\boldsymbol{n}(\boldsymbol{x})\,\mathrm{d}S_{\boldsymbol{x}}+S.P.C.(\boldsymbol{y}),\quad(2.4)$$

where

$$\boldsymbol{F}(\boldsymbol{y})=\frac{1}{\mu_e}\sum_{\beta=1}^{\tilde{N}}\int_{\tilde{S}_\beta}2\sigma k(\boldsymbol{x})\boldsymbol{n}(\boldsymbol{x})\cdot\boldsymbol{G}(\boldsymbol{r})\,\mathrm{d}S_{\boldsymbol{x}}+\boldsymbol{u}_\infty(\boldsymbol{y}),\quad(2.5)$$

$k(\boldsymbol{x})=(k_1+k_2)/2$ is the mean surface curvature at $\boldsymbol{x}\in\widetilde{S}_\beta$, and $2\sigma k\boldsymbol{n}=\boldsymbol{T}_n^e-\boldsymbol{T}_n^{int}$ is the stress jump across the interface (see, e.g. Pozrikidis 1992). The last term in (2.4), which we call $S.P.C.$ ('solid-particle contribution'), stands for additional integrals over the solid surfaces:

$$S.P.C.(\boldsymbol{y})=\sum_{\beta=1}^{\widehat{N}}\int_{\widehat{S}_\beta}\left[\frac{1}{\mu_e}\boldsymbol{G}(\boldsymbol{r})\cdot\boldsymbol{T}_n^e(\boldsymbol{x})-\boldsymbol{u}(\boldsymbol{x})\cdot\boldsymbol{\tau}(\boldsymbol{r})\cdot\boldsymbol{n}(\boldsymbol{x})\right]\mathrm{d}S_{\boldsymbol{x}} \tag{2.6}$$

(the second term in the brackets vanishes for no-slip boundary conditions). This term cannot be expressed as a sum of double-layer contributions from solid surfaces, since double-layer potentials can only describe exterior flows with zero hydrodynamic force and torque acting on solid boundaries (e.g. Odqvist 1930; Ladyzhenskaya 1969; Pozrikidis 1992), which is not the case for our problem. Representing $S.P.C.(\boldsymbol{y})$ as a sum of single-layer distributions over $\widehat{S}_\beta$ (as the form (2.6) would suggest for $\boldsymbol{u}=0$ on $\widehat{S}_\beta$) and satisfying the boundary conditions yields a system of integral equations of the second kind for $\boldsymbol{u}(\boldsymbol{x})$, but of the first kind for the potential density on the solid boundaries. This method, however, could not succeed in any of our simulations for drop squeezing between solid particles because of ill-conditioning (see § 4 for more detail) and, hence, it is not a prospective approach for emulsion flow simulations through a granular material (although there have been successful applications of the first-kind integral equation to less demanding problems in the literature).

Two alternatives for handling (2.6) have been explored in the present work. One is to use the representation of Power & Miranda (1987) for each integral in (2.6) as a double-layer distribution over $\widehat{S}_\beta$ plus additional stokeslet and rotlet contributions from the particle centre $\widehat{\boldsymbol{x}}_\beta^c$ to complete the range:

$$\int_{\widehat{S}_\beta}\boldsymbol{q}(\boldsymbol{x})\cdot\boldsymbol{\tau}(\boldsymbol{r})\cdot\boldsymbol{n}(\boldsymbol{x})\,\mathrm{d}S_{\boldsymbol{x}}+\boldsymbol{F}_\beta\cdot\boldsymbol{G}\big(\boldsymbol{y}-\widehat{\boldsymbol{x}}_\beta^c\big)-\frac{\boldsymbol{T}_\beta}{8\pi}\times\frac{\big(\boldsymbol{y}-\widehat{\boldsymbol{x}}_\beta^c\big)}{\big|\boldsymbol{y}-\widehat{\boldsymbol{x}}_\beta^c\big|^3}, \tag{2.7}$$

where the hydrodynamic force $\boldsymbol{F}_\beta$ and torque $\boldsymbol{T}_\beta$ acting on $\widehat{S}_\beta$ are related to the rigid-body projection of the potential density $\boldsymbol{q}(\boldsymbol{x})$ through the relations (in the non-dimensional form)

$$\boldsymbol{F}_\beta=\int_{\widehat{S}_\beta}\boldsymbol{q}(\boldsymbol{x})\,\mathrm{d}S,\quad \boldsymbol{T}_\beta=\int_{\widehat{S}_\beta}\big(\boldsymbol{x}-\widehat{\boldsymbol{x}}_\beta^c\big)\times\boldsymbol{q}(\boldsymbol{x})\,\mathrm{d}S. \tag{2.8}$$

Using (2.7)–(2.8) and satisfying the boundary conditions on the particle and drop surfaces yields a system of Fredholm second-kind integral equations for the potential density $\boldsymbol{q}(\boldsymbol{x})$ on $\widehat{S}_\beta$ and velocity $\boldsymbol{u}(\boldsymbol{x})$ on $\widetilde{S}_\beta$. From our experience, this approach, when combined with the new desingularization techniques of § 3, is capable of very accurate simulations of drop squeezing between solid particles for essentially supercritical conditions (when a drop moves through a constriction with relatively little resistance), even for modest drop and particle surface discretizations. Unfortunately, the major difficulty associated with (2.7) is that we could not simulate near-critical and sub-critical conditions (when a drop is trapped in a constriction for a long time, or virtually indefinitely, without being able to pass through); in all such cases, our calculations based on (2.7) were observed to crash in a relatively short time, leading to drop–solid surfaces overlapping. Note that, if the problem is solved exactly, the drop and solid surfaces would never touch (in the absence of molecular forces). This method can be generalized by introducing arbitrary factors before the integrals (2.8), but this freedom did not alleviate the difficulties.

We have found, instead, that robust simulations in the present class of problems can be made based on Hebeker's representation for $S.P.C.$ Each integral in (2.6) represents a regular Stokes flow exterior to $\widehat{S}_\beta$ and, according to Hebeker's (1986) theory (Theorem 2.1 therein), it can be uniquely represented as a combination of single-layer and double-layer distributions over $\widehat{S}_\beta$, given a proportionality factor $\eta > 0$ between the densities of the two potentials. Accordingly, we assume

$$S.P.C.(\boldsymbol{y}) = \sum_{\beta=1}^{\widehat{N}} \int_{\widehat{S}_\beta} \boldsymbol{q}(\boldsymbol{x}) \cdot [2\boldsymbol{\tau}(\boldsymbol{r}) \cdot \boldsymbol{n}(\boldsymbol{x}) + \eta \boldsymbol{G}(\boldsymbol{r})] \, \mathrm{d}S_{\boldsymbol{x}}, \tag{2.9}$$

where $\boldsymbol{q}(\boldsymbol{x})$ is a yet unknown Hebeker density, and $\eta > 0$ is an arbitrarily chosen factor. Taking the limit $\boldsymbol{y} \to \widetilde{S}_\beta$ or $\boldsymbol{y} \to \widehat{S}_\beta$ and using jump properties of the double-layer potential give a system of second-kind integral equations for $\boldsymbol{u}(\boldsymbol{x})$ and $\boldsymbol{q}(\boldsymbol{x})$. By Wielandt's deflation (Kim & Karilla 1991; Pozrikidis 1992), this system is recast in terms of $\boldsymbol{w} = \boldsymbol{u} - \kappa \boldsymbol{u}'$ (where $\kappa = (\lambda - 1)/(\lambda + 1)$ and the prime denotes the rigid-body projection of $\boldsymbol{u}$), to avoid ill-conditioning for extreme viscosity ratios $\lambda \ll 1$ or $\lambda \gg 1$. So, the coupled system of equations to be solved at each time step takes the form

$$\boldsymbol{w}(\boldsymbol{y}) = \frac{2\boldsymbol{F}(\boldsymbol{y})}{\lambda + 1} + \kappa \left[2 \sum_{\beta=1}^{\widetilde{N}} \int_{\widetilde{S}_\beta} \boldsymbol{w}(\boldsymbol{x}) \cdot \boldsymbol{\tau}(\boldsymbol{r}) \cdot \boldsymbol{n}(\boldsymbol{x}) \, \mathrm{d}S_{\boldsymbol{x}} - \boldsymbol{w}'(\boldsymbol{y}) + \frac{\boldsymbol{n}(\boldsymbol{y})}{\widetilde{S}_\alpha} \int_{\widetilde{S}_\alpha} \boldsymbol{w} \cdot \boldsymbol{n} \, \mathrm{d}S \right]$$
$$+ \frac{2}{\lambda + 1} \sum_{\beta=1}^{\widehat{N}} \int_{\widehat{S}_\beta} \boldsymbol{q}(\boldsymbol{x}) \cdot [2\boldsymbol{\tau}(\boldsymbol{r}) \cdot \boldsymbol{n}(\boldsymbol{x}) + \eta \boldsymbol{G}(\boldsymbol{r})] \mathrm{d}S_{\boldsymbol{x}} \tag{2.10}$$

on drop surfaces ($\boldsymbol{y} \in \widetilde{S}_\alpha$), and

$$\boldsymbol{q}(\boldsymbol{y}) = \boldsymbol{F}(\boldsymbol{y}) + (\lambda - 1) \sum_{\beta=1}^{\widetilde{N}} \int_{\widetilde{S}_\beta} \boldsymbol{w}(\boldsymbol{x}) \cdot \boldsymbol{\tau}(\boldsymbol{r}) \cdot \boldsymbol{n}(\boldsymbol{x}) \, \mathrm{d}S_{\boldsymbol{x}}$$
$$+ \sum_{\beta=1}^{\widehat{N}} \int_{\widehat{S}_\beta} \boldsymbol{q}(\boldsymbol{x}) \cdot [2\boldsymbol{\tau}(\boldsymbol{r}) \cdot \boldsymbol{n}(\boldsymbol{x}) + \eta \boldsymbol{G}(\boldsymbol{r})] \, \mathrm{d}S_{\boldsymbol{x}} \tag{2.11}$$

on solid surfaces ($\boldsymbol{y} \in \widehat{S}_\alpha$). The rigid-body projection in (2.10) is calculated simply as $\boldsymbol{w}'(\boldsymbol{y}) = \boldsymbol{A} + \boldsymbol{B} \times (\boldsymbol{y} - \widetilde{\boldsymbol{x}}_\alpha^c)$, where $\boldsymbol{A}$ is the average of $\boldsymbol{w}$ over the drop surface $\widetilde{S}_\alpha$, $\widetilde{\boldsymbol{x}}_\alpha^c$ is the drop surface centroid, and the vector $\boldsymbol{B}$ is calculated from the solution of a 3×3 system (Zinchenko *et al.* 1997) with a positive-definite matrix:

$$\left\{ \int_{\widetilde{S}_\alpha} \left[(\boldsymbol{x} - \widetilde{\boldsymbol{x}}_\alpha^c)^2 \boldsymbol{I} - (\boldsymbol{x} - \widetilde{\boldsymbol{x}}_\alpha^c)(\boldsymbol{x} - \widetilde{\boldsymbol{x}}_\alpha^c) \right] \mathrm{d}S \right\} \boldsymbol{B} = \int_{\widetilde{S}_\alpha} (\boldsymbol{x} - \widetilde{\boldsymbol{x}}_\alpha^c) \times \boldsymbol{w} \, \mathrm{d}S. \tag{2.12}$$

Once $\boldsymbol{w}$ is known, the interfacial velocity $\boldsymbol{u} = \boldsymbol{w} + \kappa \boldsymbol{w}'/(1 - \kappa)$ can be recovered.

As for the method based on (2.7), simple iterations (successive substitutions) are divergent for the system (2.10)–(2.11), but successful solutions are obtained by alternative iterative techniques (§ 3). In the limit of fine surface discretizations, the results are independent of the arbitrary parameter $\eta > 0$, but, in practice, η should not be set too large or too small. The limit $\eta \to \infty$ corresponds to first-kind integral equations on $\widehat{S}_\beta$, which was an unsuccessful approach in the present simulations (see § 4). The opposite limit $\eta \ll 1$ makes the representation (2.9) range-deficient and also leads to ill-conditioning, with excessive number of iterations per time step. In the

present class of problems, values of $\eta \sim \widehat{a}^{-1}$ (where $\widehat{a}$ is a characteristic size of solid particles) are close to optimal.

We have found in several tests for essentially supercritical conditions that (2.7) can provide more accurate results for drop squeezing between solid particles compared to the Hebeker reprsentation (2.9), for the same degree of drop and solid surface discretizations; however, the method based on (2.7) required a larger number of iterations per time step (1.5–2 times) compared to solving (2.10)–(2.11). A decisive advantage of the Hebeker's representation (2.9) is that it also allows for successful simulations in near-critical and subcritical ranges, when some drops are trapped in the constrictions with very small clearance between drop and solid surfaces. Moving the unknowns $\boldsymbol{w}$, $\boldsymbol{q}$ to the left-hand side, (2.10)–(2.11) can be written in the operator form $\boldsymbol{AX} = \boldsymbol{b}$ for $\boldsymbol{X} = (\boldsymbol{w},\ \boldsymbol{q})$, and all real eigenvalues of the operator $\boldsymbol{A}$ can be proved to be positive; for $\lambda \geqslant 1$, it can be shown additionally that all eigenvalues of $\boldsymbol{A}$ are real. Presumably, these spectral properties of the equations (2.10)–(2.11) (which we were not able to prove when the alternative representation (2.7) is the starting point) serve the robustness of our algorithm and provide stability of the iterative schemes. Unless otherwise stated, all the results in the present work were obtained based on the equations (2.9)–(2.11). Additional details of the algorithm are given below.

3. Numerical method

3.1. *Singularity and near-singularity subtractions*

The integrals (2.5), (2.10)–(2.11), as written, are not acceptable for numerical calculation owing to singularity in the kernels $\boldsymbol{G}(\boldsymbol{r})$ and $\boldsymbol{\tau}(\boldsymbol{r})$ at $\boldsymbol{r} = \boldsymbol{x} - \boldsymbol{y} = 0$, and so our numerical solution is preceded by singularity subtractions. Also, solid particles in a granular material may be (nearly) in contact (which is the case for some of our simulations in § 4). Moreover, in all interesting cases, large drops move through tight contrictions between solid particles with very small surface clearance. For all these reasons, we found that the success of numerical simulations in § 4 is crucially dependent on the techniques to address the singular ($\boldsymbol{x} = \boldsymbol{y}$) and near-singular ($\boldsymbol{x} \approx \boldsymbol{y}$) behaviours of the integrals (2.5), (2.10)–(2.11), and different cases (drop or particle 'self-interactions,' solid–solid interaction, solid–drop and drop–solid contributions) have to be handled individually, as described below.

Drop self-interactions

For $\boldsymbol{y}$ on a drop surface ($\boldsymbol{y} \in \widetilde{S}_\alpha$), the integrals (2.5), (2.10)–(2.11) over $\widetilde{S}_\alpha$ are transformed in a standard way:

$$\left.\begin{aligned} \int_{\widetilde{S}_\alpha} k(\boldsymbol{x})\boldsymbol{n}(\boldsymbol{x})\cdot\boldsymbol{G}(\boldsymbol{r})\,\mathrm{d}S_{\boldsymbol{x}} &= \int_{\widetilde{S}_\alpha} [k(\boldsymbol{x}) - k(\boldsymbol{y})]\boldsymbol{n}(\boldsymbol{x})\cdot\boldsymbol{G}(\boldsymbol{r})\,\mathrm{d}S_{\boldsymbol{x}}, \\ 2\int_{\widetilde{S}_\alpha} \boldsymbol{w}(\boldsymbol{x})\cdot\boldsymbol{\tau}(\boldsymbol{r})\cdot\boldsymbol{n}(\boldsymbol{x})\,\mathrm{d}S_{\boldsymbol{x}} &= 2\int_{\widetilde{S}_\alpha} [\boldsymbol{w}(\boldsymbol{x}) - \boldsymbol{w}(\boldsymbol{y})]\cdot\boldsymbol{\tau}(\boldsymbol{r})\cdot\boldsymbol{n}(\boldsymbol{x})\,\mathrm{d}S_{\boldsymbol{x}} + \boldsymbol{w}(\boldsymbol{y}) \end{aligned}\right\} \tag{3.1}$$

using the well-known integral identities for $\boldsymbol{G}$ and $\boldsymbol{\tau}$, which completely eliminates the $O(r^{-1})$ singularity of the original integrands in the left-hand side of (3.1). The regular right-hand side integrals (3.1) are calculated on an unstructured mesh of triangles on $\widetilde{S}_\alpha$ by a trapezoidal rule. In general, for any smooth function $\phi(\boldsymbol{x})$ on S,

$$\int_S \phi(\boldsymbol{x})\,\mathrm{d}S \approx \sum_i \phi\left(\boldsymbol{x}^i\right)\Delta S_i, \quad \Delta S = \tfrac{1}{3}\sum \Delta S, \tag{3.2}$$

where the summation in the second relation (3.2) is over all flat triangle areas ΔS sharing mesh vertex $\boldsymbol{x}^i$ (this simple but efficient procedure of reassigning triangle contributions to vertices is due to Rallison 1981). The rule (3.2) is applied to calculate (3.1) for all mesh nodes (vertices) $\boldsymbol{y} = \boldsymbol{y}^j \in \widetilde{S}_\alpha$, with $\boldsymbol{x}^i = \boldsymbol{y}$ excluded from the summations.

Solid self-interactions

For $\boldsymbol{y}$ on a solid surface ($\boldsymbol{y} \in \widehat{S}_\alpha$), singularity subtraction is also made:

$$\int_{\widehat{S}_\alpha} \boldsymbol{q}(\boldsymbol{x}) \cdot [2\boldsymbol{\tau}(\boldsymbol{r}) \cdot \boldsymbol{n}(\boldsymbol{x}) + \eta \mathbf{G}(\boldsymbol{r})] \, \mathrm{d}S_{\boldsymbol{x}}$$
$$= \boldsymbol{q}(\boldsymbol{y}) + \int_{\widehat{S}_\alpha} [\boldsymbol{q}(\boldsymbol{x}) - \boldsymbol{q}(\boldsymbol{y})] \cdot [2\boldsymbol{\tau}(\boldsymbol{r}) \cdot \boldsymbol{n}(\boldsymbol{x}) + \eta \mathbf{G}(\boldsymbol{r})] \, \mathrm{d}S_{\boldsymbol{x}} + \eta \boldsymbol{q}(\boldsymbol{y}) \int_{\widehat{S}_\alpha} \mathbf{G}(\boldsymbol{r}) \, \mathrm{d}S_{\boldsymbol{x}}, \quad (3.3)$$

where the first non-singular integral in the right-hand side of (3.3) is calculated on an unstructured mesh using (3.2). Unlike for drop surfaces, there is an additional integral in the right-hand side of (3.3) that must be calculated analytically or, at least, much more accurately than the first integral for the subtraction procedure (3.3) to make sense. Leaving aside the case of arbitrarily- shaped solid particles, we have developed an analytical calculation of the additional integral (3.3) for spherical and spheroidal particles (prolate and oblate); the (semi) analytical calculation can probably be done for some other shapes, including three-dimensional ellipsoids and more exotic toroidal particles. This present limitation on our techniques still appears to provide enough generality for future studies of multidrop motion through a random granular material with globular grains; assuming solid particles of more complex shapes would introduce too many parameters to make it a tractable study. For a sphere of radius a_α, the additional integral (3.3) takes a simple form

$$\int_{\widehat{S}_\alpha} \mathbf{G}(\boldsymbol{r}) \, \mathrm{d}S_{\boldsymbol{x}} = -\frac{a_\alpha^2}{2} \left[\left(1 + \frac{a_\alpha^2}{3R^2} \right) \frac{\boldsymbol{I}}{R} + \left(1 - \frac{a_\alpha^2}{R^2} \right) \frac{\boldsymbol{R}\boldsymbol{R}}{R^3} \right], \quad \boldsymbol{R} = \boldsymbol{y} - \widehat{\boldsymbol{x}}_\alpha^c \quad (3.4)$$

valid for all $R = \|\boldsymbol{R}\| \geqslant a_\alpha$ (Appendix A). For spheroidal particles (prolate and oblate), an efficient way of calculating the integral (3.4) through fast-convergent expansions in spheroidal harmonics is also given in Appendix A.

Solid–solid interactions

When the node $\boldsymbol{y}$ belongs to a solid surface $\widehat{S}_\alpha$ different from an integration surface $\widehat{S}_\beta$, we employ the general idea of 'near-singularity' subtraction (originally offered by Loewenberg & Hinch 1996 for drop–drop interaction). Namely, the solid-particle contribution (2.12) of $\widehat{S}_\beta$ is transformed as

$$\int_{\widehat{S}_\beta} \boldsymbol{q}(\boldsymbol{x}) \cdot [2\boldsymbol{\tau}(\boldsymbol{r}) \cdot \boldsymbol{n}(\boldsymbol{x}) + \eta \mathbf{G}(\boldsymbol{r})] \, \mathrm{d}S_{\boldsymbol{x}}$$
$$= \int_{\widehat{S}_\beta} [\boldsymbol{q}(\boldsymbol{x}) - \boldsymbol{q}(\boldsymbol{x}^*)] \cdot [2\boldsymbol{\tau}(\boldsymbol{r}) \cdot \boldsymbol{n}(\boldsymbol{x}) + \eta \mathbf{G}(\boldsymbol{r})] \, \mathrm{d}S_{\boldsymbol{x}} + \eta \boldsymbol{q}(\boldsymbol{x}^*) \int_{\widehat{S}_\beta} \mathbf{G}(\boldsymbol{r}) \, \mathrm{d}S_{\boldsymbol{x}}, \quad (3.5)$$

where $\boldsymbol{x}^* = \boldsymbol{x}^*(\boldsymbol{y}, \beta)$ is the mesh node (vertex) on $\widehat{S}_\beta$ that is closest to $\boldsymbol{y}$; the additonal integral (3.5) is handled analytically by (3.4) (with $\widehat{S}_\alpha$ replaced by $\widehat{S}_\beta$) for spherical particles, or by the expansions of Appendix A for spheroids. Transformation (3.5) is only essential for $\boldsymbol{y} = \boldsymbol{x} - \boldsymbol{r}$ close to $\widehat{S}_\beta$, but we apply it for all $\boldsymbol{y} \in \widehat{S}_\alpha$ to ensure smoothness of the procedure. It can be noted that, in general, (3.5) (unlike (3.3)) does

not completely eliminate singular behaviour of the integrand, but only reduces it to $O(r^{-1})$ from $O(r^{-2})$. Nevertheless, (3.5) is sufficient in the present applications, since our solid particles have no relative motion, and there are no solid–solid lubrication contributions.

Solid–drop contributions

Compared to drop–drop interactions at finite deformations (Zinchenko *et al.* 1997, 1999; Zinchenko & Davis 2000, 2002, 2003), drop squeezing between solid particles is much more lubrication sensitive. We found that the ability of a three-dimensional algorithm to simulate drop motion through tight constrictions (with inner diameter from two to several times smaller than the non-deformed drop diameter), especially for conditions not far from critical, is mostly determined by how accurately the solid–drop double-layer contribution

$$\int_{\widehat{S}_\beta} \boldsymbol{q}(\boldsymbol{x})\cdot\boldsymbol{\tau}(\boldsymbol{r})\cdot\boldsymbol{n}(\boldsymbol{x})\,\mathrm{d}S_{\boldsymbol{x}}, \quad \boldsymbol{y}=\boldsymbol{x}-\boldsymbol{r}\in\widetilde{S}_\alpha, \tag{3.6}$$

is represented for $\boldsymbol{y}$ close to $\widehat{S}_\beta$. The relatively simple idea of the leading-order near-singularity subtraction for (3.6) (as in (3.5)) did not allow our simulations to succeed, leading to a crash with drop–solid overlapping. We found instead a novel tool of *high-order near-singularity subtraction*, as detailed below, to be very promising.

In addition to the global Cartesian coordinate system (x_1, x_2, x_3), consider a local (intrinsic) coordinate system (x', y', z') centred at a mesh node $\boldsymbol{x}^i \in \widehat{S}_\beta$ with the z'-axis along the normal vector $\boldsymbol{n}(\boldsymbol{x}^i)$. The basis unit vectors of the x'- and y'-axes are $\boldsymbol{e}'_1=(e'_{11},\ e'_{12},\ e'_{13})$ and $\boldsymbol{e}'_2=(e'_{21},\ e'_{22},\ e'_{23})$, respectively, in global coordinates. The intrinsic coordinate system (x', y', z') is determined to within an arbitrary rotation about z'. Coordinates x' and y' of a surface point $\boldsymbol{x}\in\widehat{S}_\beta$ serve as a local surface parameterization near $\boldsymbol{x}^i$, and so the Hebeker density $\boldsymbol{q}(\boldsymbol{x})$ on $\widehat{S}_\beta$ may be approximated at $\boldsymbol{x}\approx\boldsymbol{x}^i$ as a first-degree polynomial in x' and y':

$$\boldsymbol{q}(\boldsymbol{x}) \approx \boldsymbol{q}(\boldsymbol{x}^i) + \boldsymbol{A}x' + \boldsymbol{B}y'. \tag{3.7}$$

The vector coefficients $\boldsymbol{A}$ and $\boldsymbol{B}$ are found by least-squares fitting of (3.7) to the values of $\boldsymbol{q}(\boldsymbol{x})$ in mesh nodes $\boldsymbol{x}^j$ directly connected to $\boldsymbol{x}^i$:

$$\sum_{j\in\mathscr{A}_i}(\boldsymbol{A}x'_j+\boldsymbol{B}y'_j-\Delta\boldsymbol{q}^j)^2\to\min, \quad \Delta\boldsymbol{q}^j=\boldsymbol{q}(\boldsymbol{x}^j)-\boldsymbol{q}(\boldsymbol{x}^i), \tag{3.8}$$

which immediately gives the equations for $\boldsymbol{A}$ and $\boldsymbol{B}$:

$$T_{11}\boldsymbol{A}+T_{12}\boldsymbol{B}=\sum_{j\in\mathscr{A}_i}x'_j\Delta\boldsymbol{q}^j, \quad T_{12}\boldsymbol{A}+T_{22}\boldsymbol{B}=\sum_{j\in\mathscr{A}_i}y'_j\Delta\boldsymbol{q}^j, \tag{3.9}$$

with

$$T_{11}=\sum_{j\in\mathscr{A}_i}(x'_j)^2, \quad T_{12}=\sum_{j\in\mathscr{A}_i}x'_jy'_j, \quad T_{22}=\sum_{j\in\mathscr{A}_i}(y'_j)^2. \tag{3.10}$$

In (3.8)–(3.10), $\mathscr{A}_i$ is the set of mesh nodes directly connected to $\boldsymbol{x}^i$ (which incudes at least five, typically six neighbours for the unstructured meshes we are using, see Zinchenko *et al.* 1997), and $x'_j=(\boldsymbol{x}^j-\boldsymbol{x}^i)\cdot\boldsymbol{e}'_1$, $y'_j=(\boldsymbol{x}^j-\boldsymbol{x}^i)\cdot\boldsymbol{e}'_2$ are intrinsic coordinates of the neighbours. Solving (3.9) and returning to the global coordinates, the linear

approximation (3.7) can be factorized as

$$\boldsymbol{q}(\boldsymbol{x}) \approx \boldsymbol{q}(\boldsymbol{x}^i) + \sum_{j\in\mathscr{A}_i} c_{k,j,i}\left(x_k - x_k^i\right)\Delta\boldsymbol{q}^j \tag{3.11}$$

(assuming summation in $k=1, 2, 3$, but no summation in i), where

$$c_{k,j,i} = \frac{(T_{22}x_j' - T_{12}y_j')e_{1,k} + (T_{11}y_j' - T_{12}x_j')e_{2,k}}{T_{11}T_{22} - (T_{12})^2} \tag{3.12}$$

and x_k, x_k^i in (3.11) are global Cartesian coordinates of $\boldsymbol{x}$ and $\boldsymbol{x}^i$, respectively. The coefficients $c_{k,j,i}$ are independent of $\boldsymbol{q}$ (and of arbitrary rotation about z') and are precalculated for all β and all $\boldsymbol{x}^i \in \widehat{S}_\beta$ before iterations.

Now, let $\boldsymbol{x}^i$ be the mesh node on $\widehat{S}_\beta$ that is closest to $\boldsymbol{y} \in \widetilde{S}_\alpha$. The integral (3.6) is regularized as

$$\int_{\widehat{S}_\beta} \left\{ \boldsymbol{q}(\boldsymbol{x}) - \boldsymbol{q}(\boldsymbol{x}^i) - \sum_{j\in\mathscr{A}_i} c_{k,j,i}\left(x_k - x_k^i\right)\left[\boldsymbol{q}(\boldsymbol{x}^j) - \boldsymbol{q}(\boldsymbol{x}^i)\right] \right\} \cdot \boldsymbol{\tau}(\boldsymbol{r}) \cdot \boldsymbol{n}(\boldsymbol{x})\, \mathrm{d}S_{\boldsymbol{x}}$$
$$+ \sum_{j\in\mathscr{A}_i} c_{k,j,i}[\boldsymbol{q}(\boldsymbol{x}^j) - \boldsymbol{q}(\boldsymbol{x}^i)] \cdot \frac{3}{4\pi}\int_{\widehat{S}_\beta} \frac{[\boldsymbol{r}\cdot\boldsymbol{n}(\boldsymbol{x})]r_k\boldsymbol{r}\boldsymbol{r}}{r^5}\, \mathrm{d}S_{\boldsymbol{x}} \tag{3.13}$$

using (2.2). In the first integral (3.13), the near-singularity of the integrand (when $\boldsymbol{y}$ is close to $\widehat{S}_\beta$) is now fully suppressed, and this integral is calculated by the trapezoidal rule (3.2). The cumbersome part with $c_{k,j,i}$ in parentheses (3.13) does not slow down iterations, if its contribution to (3.13) is represented (after applying the trapezoidal rule) as

$$\sum_{j\in\mathscr{A}_i} c_{k,j,i}\boldsymbol{\Gamma}_k(\boldsymbol{y}, \beta)[\boldsymbol{q}(\boldsymbol{x}^j) - \boldsymbol{q}(\boldsymbol{x}^i)], \tag{3.14}$$

where the 3×3 matrices $\boldsymbol{\Gamma}_k(\boldsymbol{y}, \beta)$ are independent of $\boldsymbol{q}$ and precalculated before the iterations at a modest additional expense. An additional third-rank tensor appearing in (3.13),

$$\boldsymbol{\Psi}(\boldsymbol{y}, \beta) = \frac{3}{4\pi}\int_{\widehat{S}_\beta} \frac{[\boldsymbol{r}\cdot\boldsymbol{n}(\boldsymbol{x})]\boldsymbol{r}\boldsymbol{r}\boldsymbol{r}}{r^5}\, \mathrm{d}S_{\boldsymbol{x}}, \tag{3.15}$$

is fully permutable in all three indices and can be also represented as (Appendix A)

$$\Psi_{k,\ell,m} = \frac{1}{8\pi}\left\{ (\delta_{k\ell}\nabla_m + \delta_{km}\nabla_\ell - R_\ell\nabla_k\nabla_m - R_m\nabla_k\nabla_\ell)\int_{\widehat{\mathscr{D}}_\beta} \frac{1}{r}\, \mathrm{d}V_{\boldsymbol{x}} \right.$$
$$\left. + \nabla_k\nabla_m\int_{\widehat{\mathscr{D}}_\beta} \frac{\xi_\ell}{r}\, \mathrm{d}V_{\boldsymbol{x}} + \nabla_k\nabla_\ell\int_{\widehat{\mathscr{D}}_\beta} \frac{\xi_m}{r}\, \mathrm{d}V_{\boldsymbol{x}} \right\} \tag{3.16}$$

via the integrals over the particle volume $\widehat{\mathscr{D}}_\beta$, where, for brevity, $\nabla_k = \partial/\partial y_k$, $\boldsymbol{R} = \boldsymbol{y} - \widehat{\boldsymbol{x}}_\beta^c$ and $\boldsymbol{\xi} = \boldsymbol{x} - \widehat{\boldsymbol{x}}_\beta^c$. The form (3.16) makes it easier to study $\boldsymbol{\Psi}$ analytically for some shapes. For a spherical particle $\widehat{S}_\beta$ of radius a_β centred at $\widehat{\boldsymbol{x}}_\beta^c$,

$$\Psi_{k,\ell,m} = a_\beta^3\left(\frac{a_\beta^2}{R^2} - 1\right)\frac{R_kR_\ell R_m}{R^5} - \frac{a_\beta^5}{5R^5}(\delta_{k\ell}R_m + \delta_{km}R_\ell + \delta_{\ell m}R_k). \tag{3.17}$$

We have also found closed forms for $\boldsymbol{\Psi}$ for prolate and oblate spheroids (Appendix A).

For the solid–drop single-layer contributon, a simple regularization is used:

$$\int_{\widehat{S}_\beta} \boldsymbol{q}(\boldsymbol{x})\cdot\mathbf{G}(\boldsymbol{r})\,\mathrm{d}S_x = \int_{\widehat{S}_\beta} [\boldsymbol{q}(\boldsymbol{x})-\boldsymbol{q}^*]\cdot\mathbf{G}(\boldsymbol{r})\,\mathrm{d}S_x + \boldsymbol{q}^*\int_{\widehat{S}_\beta}\mathbf{G}(\boldsymbol{r})\,\mathrm{d}S_x \tag{3.18}$$

when $\boldsymbol{y}\in\widetilde{S}_\alpha$. Although some tests suggest that a simple choice $\boldsymbol{q}^*=\boldsymbol{q}(\boldsymbol{x}^i)$ (where, again, $\boldsymbol{x}^i$ is the mesh node on $\widehat{S}_\beta$ nearest to $\boldsymbol{y}$) would suffice in the present calculations, we generally prefer a smooth form $\boldsymbol{q}^*=\boldsymbol{q}(\boldsymbol{x}_S^*)$ (where $\boldsymbol{x}_S^*$ is the surface point on $\widehat{S}_\beta$ nearest to $\boldsymbol{y}$), to avoid noticeable discontinuity for $\boldsymbol{q}^*$ in dynamical simulations. The value of $\boldsymbol{q}^*$ has to be found by interpolation. Since $\boldsymbol{y}-\boldsymbol{x}_S^*$ is approximately parallel to $\boldsymbol{n}(\boldsymbol{x}^i)$, relations (3.11)–(3.12) yield

$$\boldsymbol{q}^* = \boldsymbol{q}(\boldsymbol{x}^i) + \sum_{j\in\mathscr{A}_i} c_{k,j,i}\left(y_k - x_k^i\right)\Delta\boldsymbol{q}^j. \tag{3.19}$$

The additional integral in (3.18), handled analytically, has already appeared in (3.5).

Drop–solid and drop–drop contributions

For the single-layer integrals (2.5), when $\boldsymbol{y}$ lies on a solid, or another drop surface $\widetilde{S}_\alpha\neq\widetilde{S}_\beta$, a smooth near-singualrity subtraction is also recommended:

$$\int_{\widetilde{S}_\beta} k(\boldsymbol{x})\boldsymbol{n}(\boldsymbol{x})\cdot\mathbf{G}(\boldsymbol{r})\,\mathrm{d}S_x = \int_{\widetilde{S}_\beta} [k(\boldsymbol{x})-k(\boldsymbol{x}_S^*)]\boldsymbol{n}(\boldsymbol{x})\cdot\mathbf{G}(\boldsymbol{r})\,\mathrm{d}S_x, \tag{3.20}$$

where $\boldsymbol{x}_S^*$ is the surface point on $\widetilde{S}_\beta$ closest to $\boldsymbol{y}$. The expression for $k(\boldsymbol{x}_S^*)$ is similar to (3.19)

$$k(\boldsymbol{x}_S^*) = k(\boldsymbol{x}^i) + \sum_{j\in\mathscr{A}_i} c_{m,j,i}\left(y_m - x_m^i\right)[k(\boldsymbol{x}^j)-k(\boldsymbol{x}^i)], \tag{3.21}$$

with $\boldsymbol{x}^i$ being the mesh node on $\widetilde{S}_\beta$ nearest to $\boldsymbol{y}$, and $\mathscr{A}_i$ its set of neighbours. Here, it is important to use $k(\boldsymbol{x}_S^*)$ instead of common $k(\boldsymbol{x}^i)$ (otherwise, some of our simulations crash in the subcritial range, when a drop is trapped in a constriction).

Quite different is our technique of near-singularity subtraction for the double-layer drop contribution:

$$\int_{\widetilde{S}_\beta} \boldsymbol{w}(\boldsymbol{x})\cdot\boldsymbol{\tau}(\boldsymbol{r})\cdot\boldsymbol{n}(\boldsymbol{x})\,\mathrm{d}S_x = \int_{\widetilde{S}_\beta} [\boldsymbol{w}(\boldsymbol{x})-\boldsymbol{w}^*]\cdot\boldsymbol{\tau}(\boldsymbol{r})\cdot\boldsymbol{n}(\boldsymbol{x})\,\mathrm{d}S_x, \quad \boldsymbol{y}\notin\widetilde{S}_\beta. \tag{3.22}$$

The simplest choice $\boldsymbol{w}^*=\boldsymbol{w}(\boldsymbol{x}^i)$ was unsatisfactory in some simulations with contrast viscosities (e.g. $\lambda=0.25$) in the near-critical range, leading to divergence of iterations and/or surface overlapping, but the idea of high-order near-singularity subtraction was not productive either in this case. We found instead that a significant improvement over the standard choice $\boldsymbol{w}^*=\boldsymbol{w}(\boldsymbol{x}^i)$ in the present simulations is provided by the variational method of Zinchenko & Davis (2002), which requires the subtracted quantity $\boldsymbol{w}^*$ to minimize the Euclidean norm of the discretized double layer (3.22) for a given $\boldsymbol{y}$,

$$\sum_{\boldsymbol{x}^j\in\widetilde{S}_\beta} \frac{[\boldsymbol{r}\cdot\boldsymbol{n}(\boldsymbol{x}^j)\Delta S_j]^2[\boldsymbol{r}\cdot(\boldsymbol{w}(\boldsymbol{x}^j)-\boldsymbol{w}^*)]^2}{r^8} \to \min, \quad \boldsymbol{r}=\boldsymbol{x}^j-\boldsymbol{y}, \tag{3.23}$$

which gives a linear 3×3 system of equations for $\boldsymbol{w}^*$:

$$\left[\sum_{\boldsymbol{x}^j \in \widetilde{S}_\beta} \frac{[\boldsymbol{r} \cdot \boldsymbol{n}(\boldsymbol{x}^j) \Delta S_j]^2 \boldsymbol{r}\boldsymbol{r}}{r^8} \right] \boldsymbol{w}^* = \sum_{\boldsymbol{x}^j \in \widetilde{S}_\beta} \frac{[\boldsymbol{r} \cdot \boldsymbol{n}(\boldsymbol{x}^j) \Delta S_j]^2 [\boldsymbol{r} \cdot \boldsymbol{w}(\boldsymbol{x}^j)] \boldsymbol{r}}{r^8}. \tag{3.24}$$

Although the scheme (3.24) looks complicated, it can be implemented efficiently: the subtracted part in the discretized right-hand side integral (3.22) is calculated as $\boldsymbol{D}^T$ times the right-hand side of (3.24), where the matrices

$$\boldsymbol{D}(\boldsymbol{y}, \beta) = \frac{3}{4\pi} \left[\sum_{\boldsymbol{x}^j \in \widetilde{S}_\beta} \frac{[\boldsymbol{r} \cdot \boldsymbol{n}(\boldsymbol{x}^j) \Delta \boldsymbol{S}_j]^2 \boldsymbol{r}\boldsymbol{r}}{r^8} \right]^{-1} \sum_{\boldsymbol{x}^j \in \widetilde{S}_\beta} \frac{\boldsymbol{r} \cdot \boldsymbol{n}(\boldsymbol{x}^j) \Delta \boldsymbol{S}_j \boldsymbol{r}\boldsymbol{r}}{r^5} \tag{3.25}$$

are precalculated before the iterations for all $\boldsymbol{y}$ and β.

Even though the numerical calculations in the present work were for one drop squeezing between several solid particles, our experience with purely multidrop systems (Zinchenko & Davis 2002) suggests that (3.24) is also a recommended choice for the subtracted quantity $\boldsymbol{w}^*$ in the case of drop–drop contribution (3.22), should there be more than one drop interacting with solid obstacles.

The variety of different near-singularity subtraction schemes discussed above should not be confusing. We have found it impossible to use some unified subtraction scheme for all types of surface-to-surface boundary-integral contributions in a robust algorithm. For example, using high-order near-singularity subtraction for solid–solid interaction instead of (3.5) made the convergence of iterations much slower when solid particles are (nearly) in contact, without significant accuracy improvement, and could not be accepted. Moreover, when high-order subtraction was included in the solid–drop single-layer contributon, instead of (3.18), the algorithm lost the ability to simulate the trapped steady state of a drop in a constriction and led to a crash at large times (much larger, though, than in the simulations based on the representation (2.7)–(2.8) of Power & Miranda 1987). On the other hand, high-order subtraction in the double-layer solid–drop contribution (3.13) was most crucial for successful simulations in § 4 and could not be replaced, for example, by the variational technique in the spirit of (3.22)–(3.24). Overall, we found the choice of suitable desingularization techniques working in a broad range of conditions to be highly non-trivial in this problem (which may be due to different behaviour of $\boldsymbol{q}(\boldsymbol{x})$ and $\boldsymbol{w}(\boldsymbol{x})$ in near-contact areas), and it is based on our extensive experimenting rather than on rational logic.

3.2. *Additional features of the algorithm*

To calculate curvature $k(\boldsymbol{x}^i)$ and the normal vector $\boldsymbol{n}(\boldsymbol{x}^i)$ in the nodes of an unstructured mesh of triangles on a drop, we use fourth-order local fitting to the drop surface in a coordinate system with the z-axis along the normal vector, and two layers of mesh nodes around $\boldsymbol{x}^i$. Such an algorithm, outlined in Appendix B, is a simple variation of the best-paraboloid method of Zinchenko *et al.* (1997) and was found to describe the dynamics of drop squeezing through tight constrictions somewhat more accurately in the present calculations. It should be noted, though, that this algorithm, in general, is less robust than the best-paraboloid method, in that it is less capable of simulating very elongated drop shapes approaching breakup (when our fixed topology mesh becomes highly stretched). This difficulty, however, was irrelevant to the present calculations with compact shapes, as discussed in § 4 in more detail. There are efficient ways of topological mesh restructuring (Cristini

et al. 1998, 2001) into compact triangles, which could make the high-order curvature scheme more robust, but we did not try to explore whether such a combination of the two approaches would be beneficial in breakup simulations.

A traditional method of simple iterations (successive substitutions) is divergent for the boundary-integral system of equations (2.10)–(2.11). An alternative technique of biconjugate-gradient iterations is successful, but requires an adjoint operator, which complicates the code. We have found in the present simulations that, for moderate viscosity ratios λ, a simpler generalized minimal-residual method GMRES(k) is competitive. As in multidrop shear-flow simulations (Zinchenko & Davis 2002), $k=2$ was found to be close to optimum. For $\lambda=O(1)$, the number of iterations to maintain the residual of the equations (2.10)–(2.11) within 10^{-5} for all mesh nodes ranges from 2–4 (when a drop is away from the constriction, or has reached a trapped state) to 8–10 (when the drop moves vigorously through a tight constriction). Contrast viscosities ($\lambda=10$) required slightly more iterations. Unlike for pure drop systems, the case $\lambda=1$ still requires an iterative solution.

For solid surfaces, we used stationary unstructured triangulations, with moderate adaptation to the constriction region when necessary (§4 and Appendix C). For deformable drops, we started from spherical shapes and initial uniform unstructured triangulations prepared in a standard way from regular polyhedra by a series of refinements (Kim & Karilla 1991; Zinchenko & Davis 2004). To avoid a familiar difficulty with mesh degradation, as a drop moves and deforms, a version (Zinchenko & Davis 2002, 2003) of 'passive mesh stabilization' was used to maintain the quality of fixed topology surface triangulation by adding a suitable tangential field on the drop surface. This field is found iteratively at each time step by minimizing the 'kinetic mesh energy' (in the form (A 1) of Zinchenko & Davis 2002 at $\alpha=2$), to prevent mesh triangle collapse and the internode distances from becoming irregular in long-time simulations. This relatively simple, curvature-nonadaptive version is very robust in the present simulations, where drops experience complex shape transformations, but remain compact. We expect, though, that for higher capillary numbers, when the drop develops high curvature upon leaving the constriction, curvature-adaptive meshing would be required; such adaptation would still be possible for fixed-topology triangulations (Zinchenko & Davis 2000).

Several thousand triangular elements were typically used on each drop and solid surface. Drop shapes were updated by the second-order Runge–Kutta scheme. A stable yet economical time step Δt was chosen empirically as

$$\Delta t = K_{\Delta t}\frac{\mu_e}{\sigma}\min_i\left\{\frac{\Delta x_i}{\widetilde{a}\max[|k_1(\boldsymbol{x}^i)|,\,|k_2(\boldsymbol{x}^i)|]}\right\}. \tag{3.26}$$

Here, $K_{\Delta t}=O(1)$ is a non-dimensional numerical factor, the minimum is taken over all mesh nodes $\boldsymbol{x}^i$ on the drop surface, Δx_i is the minimum distance from $\boldsymbol{x}^i$ to its neighbours on the drops surface, $\widetilde{a}$ is the non-deformed drop radius, and k_1, k_2 are the principal curvatures at $\boldsymbol{x}^i$ (should there be more than one drop, the minimum of (3.26) is additionally taken over all drops). The form (3.26) becomes the usual limitation $\Delta t \leqslant K_{\Delta t}\mu_e \min|\Delta x_i|/\sigma$ (Rallison 1981) for a spherical drop. For the present calculations with $Ca=0(1)$, we found that we could use larger values of $K_{\Delta t}$, from 3.5 for $\lambda=0.25$ to 7–9 for $1\leqslant\lambda\leqslant 10$, than those for $Ca\ll 1$ and nearly spherical drops (Zinchenko & Davis 2005). In principle, when the drop comes close to solid surfaces (or other drops), there should be an additonal limitation like $\Delta t \leqslant O(K_{\Delta t}\mu_e \min\rho/\sigma)$, where $\min\rho$ is the minimum of internode distances (drop–solid, drop–drop), but excluding pairs $(\boldsymbol{x}^i,\ \boldsymbol{x}^j)$ for which $\boldsymbol{x}^j$ is the nearest node to $\boldsymbol{x}^i$ or vice

versa, as observed recently for $Ca \ll 1$ drop interactions (Zinchenko & Davis 2005). However, in the present calculations with fairly large deformations, such a limitation was absorbed by (3.26).

Finally, the drop shape was rescaled at each time step about the drop centroid $\widetilde{\boldsymbol{x}}^c$ to keep the volume constant. This common procedure helped to reduce the long-time cumulative error, with a negligible effect in the limit of fine triangulations.

4. Numerical results

In the numerical calculations below for a single, freely suspended drop motion past a group of identical solid particles rigidly held in a uniform flow $\boldsymbol{u}_\infty = \text{constant}$, we used the particle radius $\widehat{a}$ (for spheres) or the major half-axis (for spheroids) as a characteristic length scale L; the velocity and time scales are $|\boldsymbol{u}_\infty|$ and $L/|\boldsymbol{u}_\infty|$, respectively. The Hebeker parameter η in the non-dimensionalized equations (2.10)–(211) was set to 1. The capillary number is defined as

$$Ca = \frac{\mu_e|\boldsymbol{u}_\infty|}{\sigma}\,\frac{\widetilde{a}}{L} \tag{4.1}$$

(the inclusion of the drop radius $\widetilde{a}$ is, at least, motivated for $\widetilde{a}/L \ll 1$, since $|\boldsymbol{u}_\infty|/L$ is the velocity gradient estimate). The drop always started far upstream from the spherical shape. All the calculations have been performed on single-processor AMD PCs, with Athlon XP2600+ and XP3000+ CPU.

4.1. *Tests*

The main calculations were preceded by several tests to validate different parts of the code. First, we calculated the hydrodynamic force $\boldsymbol{F}$ (related to the integral of the Hebeker function $\boldsymbol{q}(\boldsymbol{x})$, e.g. Hebeker 1986) on each of the two solid spheres in near-contact in the absence of the drop, to compare with exact bispherical-coordinate solutions of Stimson & Jeffrey (1926) and O'Neill & Majumdar (1970). When the flow $\boldsymbol{u}_\infty$ is along the line-of-centres, the exact values of $|\boldsymbol{F}|/(6\pi\mu_e\widehat{a}|\boldsymbol{u}_\infty|)$ are 0.6566 and 0.6457 for the dimensionless gap of $\varepsilon = 0.2$ and 0.01, respectively; these numbers agree very well with 0.6562 and 0.6454 by the present code with $\widehat{N}_\triangle = 8640$ triangular elements per surface (non-adaptive). When the flow $\boldsymbol{u}_\infty$ is normal to the line-of-centres, the exact results are 0.7413 and 0.7255 for $\varepsilon = 0.2$ and 0.01, respectively, and are again in excellent agreement with 0.7409 and 0.7251 produced by our code with $\widehat{N}_\triangle = 8640$.

In the second series of tests, a head-on approach of a slightly deformable freely suspended drop to a single stationary solid sphere was considered. The non-dimensional non-deformed drop radius $\widetilde{a}$ and the initial gap were 0.7 and 0.4, respectively. The drop velocity $\boldsymbol{U}$ at any instant of time was calculated as the volume-averaged fluid velocity inside the drop using the Gauss theorem:

$$\boldsymbol{U} = \langle \boldsymbol{u} \rangle = \frac{1}{\widetilde{V}} \int_{\widetilde{S}} (\boldsymbol{u}\cdot\boldsymbol{n})(\boldsymbol{x} - \widetilde{\boldsymbol{x}}^c)\,\mathrm{d}S, \tag{4.2}$$

where $\widetilde{V}$ is the drop volume. On the other hand, using the 'nominal gap' $\delta = |\widehat{\boldsymbol{x}}^c - \widetilde{\boldsymbol{x}}^c| - 1 - \widetilde{a}$ as the gap between the solid sphere and the non-deformed drop with the same centroid $\widetilde{\boldsymbol{x}}^c$ (as for the deformable drop), the drop velocity can be calculated theoretically from the bispherical-coordinate solution for two spherical drops (Zinchenko 1983) in the limit when one drop viscosity is infinite. Comparison between our boundary-integral (solid line) and theoretical (dashed line) results is

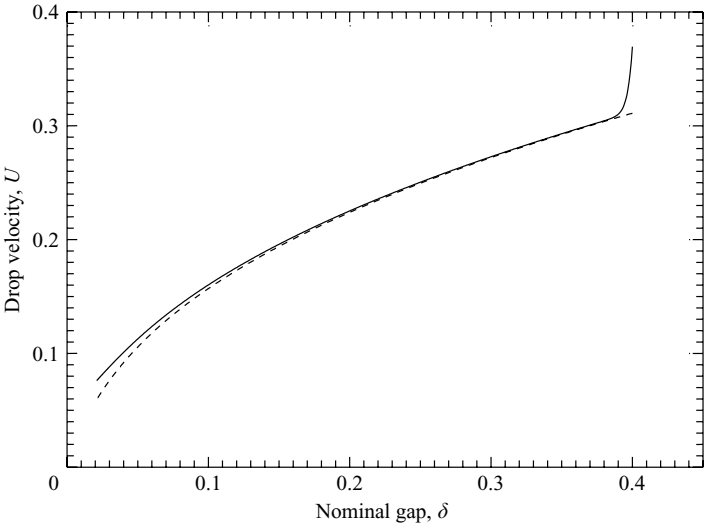

FIGURE 2. Drop velocity for head-on approach toward a stationary solid sphere for $\lambda = 0.25$ and $Ca = 5.6 \times 10^{-3}$. Solid line: boundary-integral solution ($\widetilde{N}_{\triangle} = \widehat{N}_{\triangle} = 8640$); dashed line: bispherical-coordinate solution for a spherical drop.

given in figure 2 for $\lambda = 0.25$ and $Ca = 5.6 \times 10^{-3}$; the solid line is mesh-independent. After a short relaxation time $t \sim Ca$, excellent agreement with theory is observed in a wide range of separations, until the nominal gap becomes small and deviations inevitably occur; a similar successful test was made for $\lambda = 10$ and $Ca = 2.8 \times 10^{-3}$. These $Ca \ll 1$ tests are non-trivial in that small $O(Ca)$ shape deviations from spherical in the boundary-integral solution are divided by Ca to produce an $O(1)$-effect (after the initial relaxation time $t \sim Ca$); adequate resolution and very small time steps are required.

Additionally, we checked that, when the solid particles are absent and the uniform far-field flow is replaced by a shear flow, our large-deformation stationary solutions for a single drop are consistent with those available elsewhere (e.g. Rallison 1981; Kennedy, Pozrikidis & Skalak 1994).

4.2. *Two-sphere constrictions*

Figures 3 and 4 illustrate our simulation for a drop squeezing through a tight constriction between two solid spheres at $\lambda = 4$ and $Ca = 0.63$. The uniform flow $\boldsymbol{u}_{\infty}$ and the particle line-of-centres are perpendicular and form a plane π (plane of drawing in figure 3). Symmetric initial conditions were chosen, so that the drop centre at $t = 0$ was in the plane π, at equal distances from both particles, and six units away from the particle line-of-centres. If the problem is solved exactly for such initial conditions, the drop centre should remain in the plane π along the bisector to the particle line-of-centres, and the drop shape should be symmetric about the π-plane. To preserve symmetry to high accuracy without any forcing, we used $\widetilde{N}_{\triangle} = 8640$ triangular elements on the drop and $\widehat{N}_{\triangle} = 5120$ elements on each solid sphere (non-adaptive meshes, figure 3). The non-deformed drop diameter $2\widetilde{a} = 1.8$ is almost four times larger than the gap $\varepsilon = 0.5$ between the particles, and so squeezing would require significant deformation and resistance. The snapshots in figure 4 show that the drop is able to pass the constriction without the loss of symmetry; the drop surface becomes dimpled by the solid spheres and forms a 'collar' around the constriction

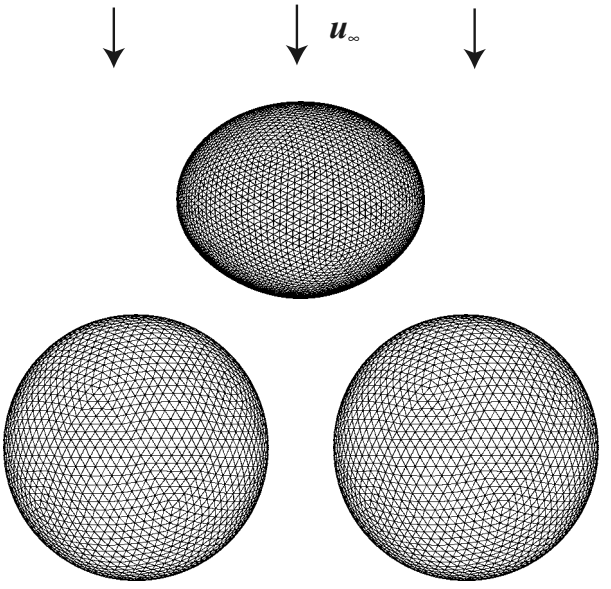

FIGURE 3. A schematic for a drop squeezing through a two-sphere constriction at $\varepsilon = 0.5$, $\tilde{a} = 0.9$, $\lambda = 4$, $Ca = 0.63$, with $\tilde{N}_\triangle = 8640$ triangular elements on the drop and $\hat{N}_\triangle = 5120$ elements on each solid sphere. The drop shape and position are shown at $t = 10$.

in the flow direction until squeezing occurs, and the drop eventually returns to the spherical shape far downstream. The snapshot of the drop mesh during squeezing (figure 5, view along the particle line-of-centres) shows that our fixed topology mesh algorithm is robust in such simulations, where the drop undergoes complex shape transformations, but remains compact.

To study the effect of drop deformability on the squeezing process, the simulation in figure 4 was repeated for several different capillary numbers. In figure 6, the non-dimensional drop velocity U (which is defined and calculated as the volume average (4.2), with the only component along $\boldsymbol{U}_\infty$) is shown *vs.* time; the most accurate calculations (for fine triangulations) are represented by solid lines. All curves start from drop velocity U slightly less than 1, owing to large but finite initial separation. For $Ca = 0.63$, the drop velocity reaches a minimum of 0.046 in the constriction before it approaches unity far downstream. For $Ca = 0.36$, the drop even decelerates about 140 times, but it is still able to pass. For all the pass-through cases, $Ca = 0.63$, 0.45 and 0.36, squeezing occurs in the manner of figure 4 without the loss of symmetry, and there is the second, local minimum of drop velocity $U(t)$ shortly before the drop leaves the constriction.

The case $Ca = 0.225$ is markedly different. The drop velocity U reaches extremely small values $U \sim 0.0003$ by $t \sim 40$ (and $\sim 10^{-6}$ by $t \sim 60$) and is believed to asymptote to zero at $t \to \infty$. The normal velocities $\boldsymbol{u} \cdot \boldsymbol{n}$ everywhere on the drop surface also become virtually zero, and the drop reaches a moderately deformed symmetrical steady shape without being able to pass the constriction. Additional calculations show that $Ca = 0.225$ is close to critical for squeezing to occur without loss of symmetry.

Figure 7 shows the temporal dynamics of the gap between the drop and solid surfaces for $Ca = 0.225$, as this trapped steady state is approached. Without numerical errors, the drop would be at equal distances from both spheres at any $t > 0$; in calculations, however, these gaps were slightly different (typically, by a few per cent

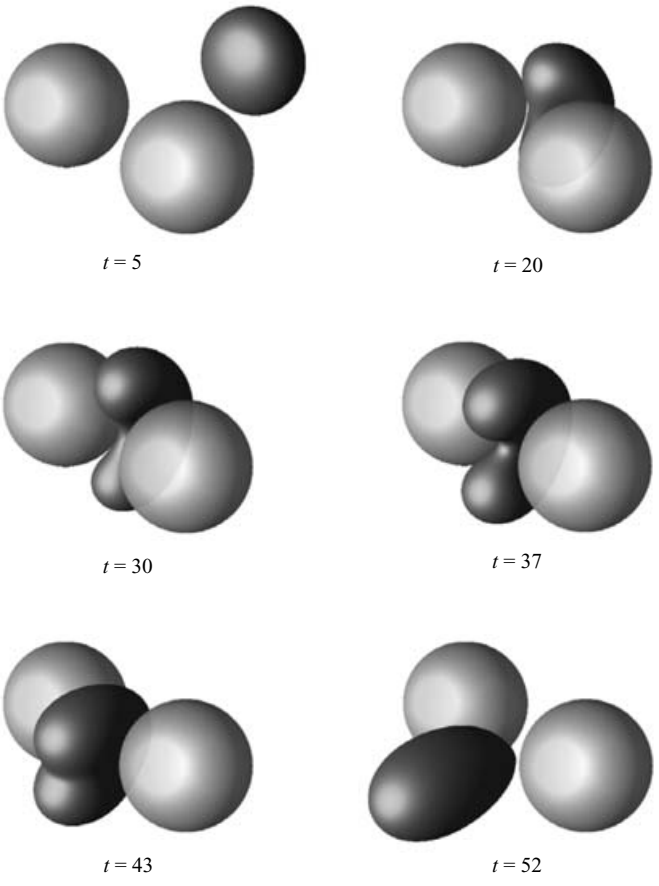

FIGURE 4. Snapshots of the drop motion through a two-sphere constriction at $\varepsilon = 0.5$, $\widetilde{a} = 0.9$, $\lambda = 4$, $Ca = 0.63$, $\widetilde{N}_{\triangle} = 8640$, $\widehat{N}_{\triangle} = 5120$; a perspective view. The calculation required 1000 time steps between $t = 20$ and $t = 43$.

in close contact), and figure 7 represents the average of the two *vs.* time. Each gap was rigorously calculated as a distance between the drop mesh polyhedron (with flat triangulation) and a particle centre minus one. Both crude (dashed line) and more accurate (solid line) resolutions demonstrate that a steady state is closely reached by $t \sim 60$, with a stationary gap ~ 0.02. Unlike for the gap, the global trapped configuration and the global steady-state drop shape were found to be practically mesh-independent. We did not attempt to extend the calculations in figure 7 to even larger times, since this stationary regime, with the symmetrical drop shape, is not expected to be asymptotically stable at $t \to \infty$ to initial conditions. In contrast, for essentially supercritical *Ca*, slight perturbation of the initial conditions does not have an appreciable effect on the squeezing process. For example, at $Ca = 0.63$, the shift in the initial position of the drop centre off the π-plane by 0.005 resulted in some subsequent loss of symmetry, with the deviation of the drop centroid from the π-plane reaching a maximum of 0.13 during squeezing. However, the whole trajectory for the drop velocity $U(t)$ along the flow direction was graphically indistinguishable from that shown in figure 6 at $Ca = 0.63$.

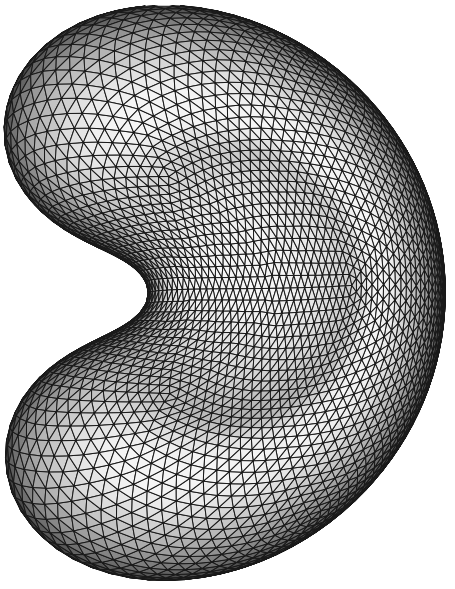

FIGURE 5. Snapshot of the drop mesh at $t = 37$ during its motion through the two-sphere constriction ($\varepsilon = 0.5$, $\widetilde{a} = 0.9$, $\lambda = 4$, $Ca = 0.63$, $\widetilde{N}_{\triangle} = 8640$, $\widehat{N}_{\triangle} = 5120$).

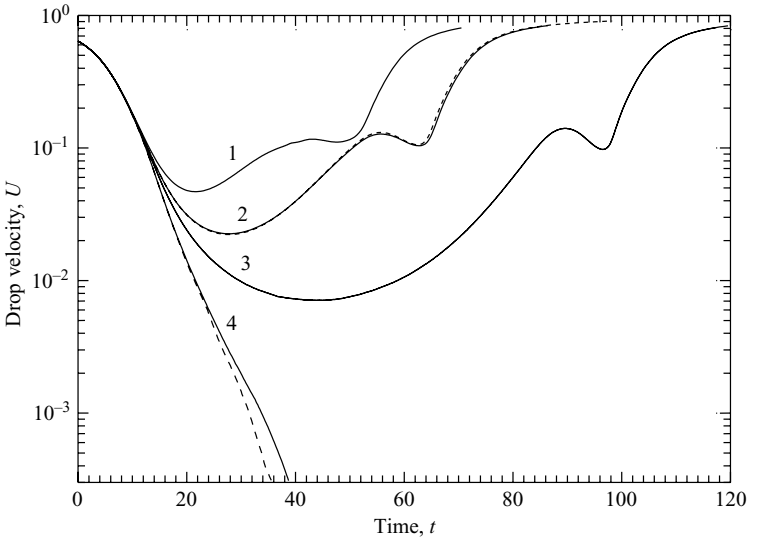

FIGURE 6. Drop velocity for its motion through the two-sphere constriction ($\varepsilon = 0.5$, $\widetilde{a} = 0.9$, $\lambda = 4$). Solid lines 1: $Ca = 0.63$, $\widetilde{N}_{\triangle} = 8640$, $\widehat{N}_{\triangle} = 5120$; 2: $Ca = 0.45$, $\widetilde{N}_{\triangle} = 8640$, $\widehat{N}_{\triangle} = 5120$; 3: $Ca = 0.36$, $\widetilde{N}_{\triangle} = 11\,520$, $\widehat{N}_{\triangle} = 8640$; 4: $Ca = 0.225$, $\widetilde{N}_{\triangle} = 11\,520$, $\widehat{N}_{\triangle} = 8640$. Short-dashed ($Ca = 0.45$, $\widetilde{N}_{\triangle} = 5120$, $\widehat{N}_{\triangle} = 3840$) and long-dashed ($Ca = 0.225$, $\widetilde{N}_{\triangle} = 8640$, $\widehat{N}_{\triangle} = 5120$) lines show the triangulation effect, which is negligible for $U \geqslant 0.005$.

Presumably, there is a qualitative analogy (M. Loewenberg, personal communication) between the trapped steady state found here for $Ca = 0.225$ and the axisymmetrical stationary solutions for a deformable drop near a plane wall and for two drops pressed together by a compressional flow (Nemer 2003; Nemer *et al.* 2004).

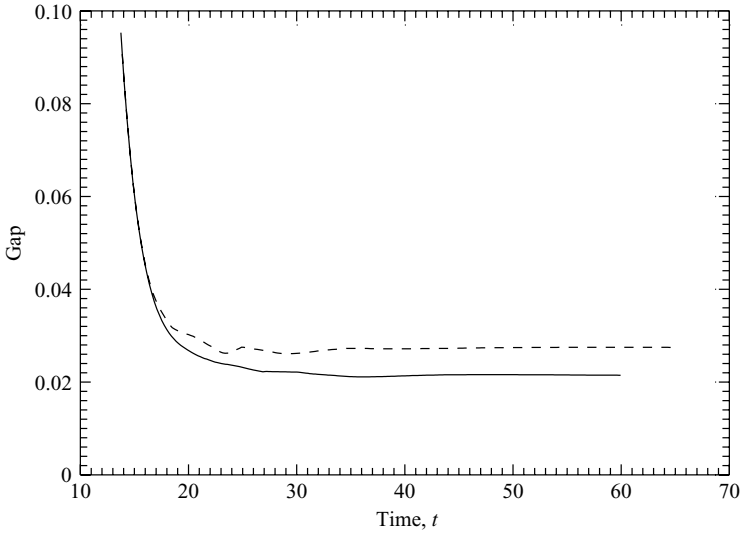

FIGURE 7. The temporal dynamics of the drop-solid spacing for $Ca = 0.225$, as the trapped steady state is approached for a two-sphere constriction ($\varepsilon = 0.5$, $\widetilde{a} = 0.9$, $\lambda = 4$). Solid line: $\widetilde{N}_{\triangle} = 11\,520$, $\widehat{N}_{\triangle} = 8640$; dashed line: $\widetilde{N}_{\triangle} = 8640$, $\widehat{N}_{\triangle} = 5120$.

In all the cases, the steady state with non-zero gap thickness is due to the local pumping flow along the drop surface, which drives fluid into the gap(s) to balance the squeezing effect of the outer flow. Nemer (2003) and Nemer *et al.* (2004) found analytically that their stationary gap has a strong scaling Ca^3, as $Ca \to 0$. An extension of their theory to the present three-dimensional problem should be possible at $Ca \ll 1$, provided that the asymptotics of the tangential stress on the spherical drop surface in near-contact regions is determined; the details may be very non-trivial, though. Even harder would be to obtain the scaling information from deformable drop simulations, owing to extreme difficulties of three-dimensional boundary-integral calculations at $Ca \ll 1$ with close interactions (Zinchenko & Davis 2005). We explored instead, at finite deformations, how the surface clearance between the drop and solid particles in the squeezing process is affected by the capillary number in the supercritical range $Ca > Ca_{crit}$ for symmetric initial conditions. The effect is surprisingly weak (figure 8); even at a substantially supercritical value of $Ca = 0.63$, the drop has to nearly coat the solid surfaces, with very small clearance, to be able to pass the tight constriction. The second minimum in the gap, observed just before the drop leaves the constriction, is reminiscent of a similar finding, from both numerical calculations and asymptotic lubrication theory, for near-contact motion of two drops at $Ca \ll 1$ (Zinchenko & Davis 2005).

4.3. *Drop squeezing between two disks*

To check the capabilities of our algorithm for non-spherical particles and demonstrate usefulness of the formulae given in Appendix A, we simulated drop squeezing between two parallel disks. Each solid particle is now an oblate spheroid with major and minor axes of 1 and 0.4, respectively; the minor axis is along the line-of-centres. Symmetric initial conditions were chosen again, with the drop centre in the π-plane, at equal distances from both particles and six units away from the particle line-of-centres. The constriction is tight in that the non-deformed drop diameter $2\widetilde{a}$ is three times larger than the gap $\varepsilon = 0.5$ between the spheroids. The snapshots of the simulation

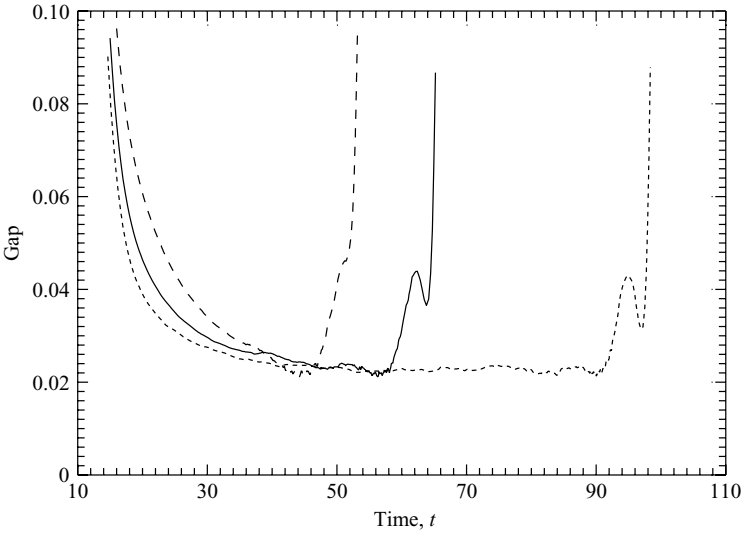

FIGURE 8. The drop–solid spacing for supercritical capillary numbers and a two-sphere constriction ($\varepsilon = 0.5$, $\widetilde{a} = 0.9$, $\lambda = 4$). Long-dashed line: $Ca = 0.63$, $\widetilde{N}_{\triangle} = 8640$, $\widehat{N}_{\triangle} = 5120$; Solid line: $Ca = 0.45$, $\widetilde{N}_{\triangle} = 8640$, $\widehat{N}_{\triangle} = 5120$; Short-dashed line: $Ca = 0.36$, $\widetilde{N}_{\triangle} = 11\,520$, $\widehat{N}_{\triangle} = 8640$.

with $\lambda = 1$, $Ca = 0.4$ and non-adaptive meshes (medium resolution) are shown in figure 9. The drop, again, passes through the constriction in a symmetric fashion, with a heart-like shape; the drop velocity U slows down up to 60 times during squeezing. Upon leaving the constriction, the drop develops a wedge-like shape (figure 9 at $t = 68.6$), with the edge (the region of curvature $k \approx 4.5\widetilde{a}^{-1}$) along the particle line-of-centres, but it slowly returns to the spherical shape far downstream. Comparison of the low-resolution (dashed line) and medium-resolution (solid line) results for the drop velocity (figure 10*a*) shows very good accuracy in the entire time range; presumably, excellent convergence is achieved because the conditions are not very close to critical in this case. The results for the gap between the drop and solids are also reasonably convergent in the entire near-contact range, the closest separation being 0.012 (figure 10*b*). The success of these simulations, as of those in § 4.2, is crucially dependent on the novel, high-order near-singularity subtraction in the double-layer solid–drop contribution (3.13). When the high-order terms were disabled (by setting $c_{k,j,i} = 0$ in (3.13)), both low-resolution ($\widetilde{N}_{\triangle} = 5120$, $\widehat{N}_{\triangle} = 3840$) and medium-resolution ($\widetilde{N}_{\triangle} = 8640$, $\widehat{N}_{\triangle} = 5120$) runs faltered very early, at $t \approx 20$–24, with drop–solid overlapping, when the drop just enters the constriction.

4.4. *Three-sphere constriction*

Here, we discuss simulations of drop squeezing between three rigidly-held solid spheres. We first consider cases where the spheres are separated, and then provide additional results for the spheres essentially in contact. In all cases, the particles of unit radius form an equilateral triangle, and the uniform flow $\boldsymbol{u}_{\infty}$ is normal to the plane of particle centers. The drop centre is placed initially upstream six units away from this plane, and aimed at the constriction centre (figure 11). For a small-to-moderate spacing ε between solid particles, we found it advantageous to use particle meshing moderately adaptive to the distance from the constriction centre (not to near-contact areas between solids). A simple algorithm for such adaptation is given in Appendix C.

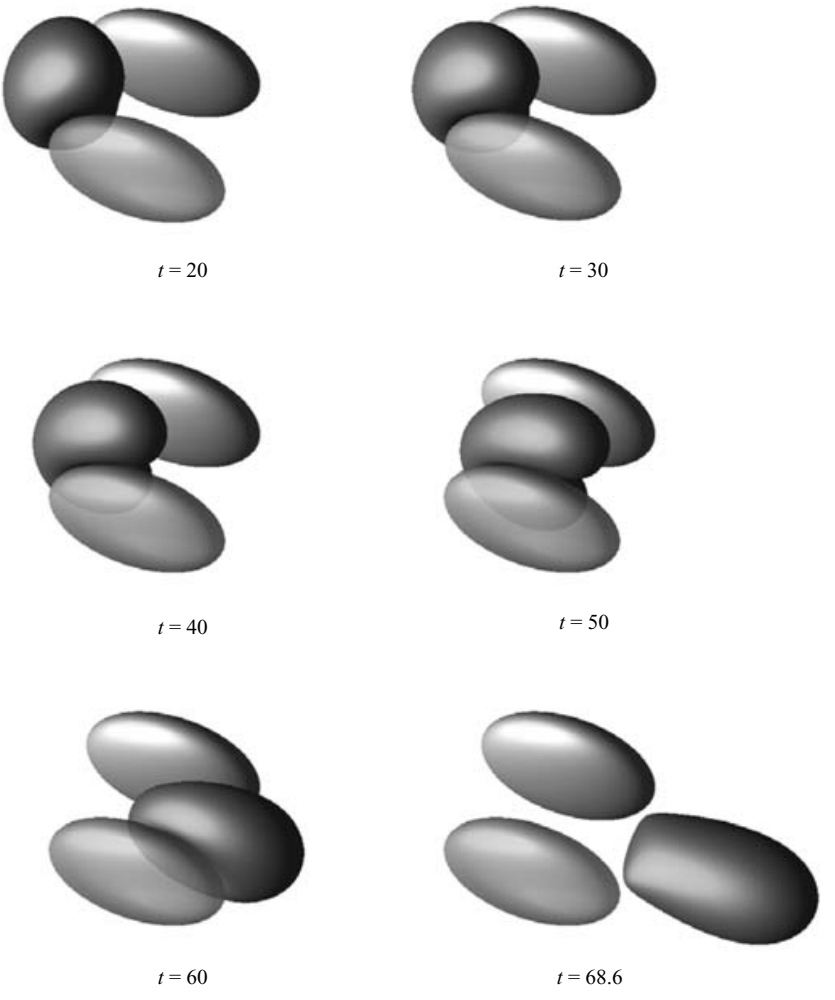

FIGURE 9. Snapshots of the drop motion between two parallel disks ($\varepsilon = 0.5$, $\widetilde{a} = 0.75$, $\lambda = 1$, $Ca = 0.4$, $\widetilde{N}_{\triangle} = 8640$, $\widehat{N}_{\triangle} = 5120$); a perspective view.

Figure 12 presents snapshots of the simulation for $\varepsilon = 0.25$, $\widetilde{a} = 0.6$, $\lambda = 4$, $Ca = 1.3$, and medium resolution. The constriction is tight, with the non-deformed drop diameter $2\widetilde{a}$ being about twice as large as the inner diameter of the hole. The drop squeezes through the hole extremely slowly, decelerating up to 500 times, but it is still able to pass through. Figure 13 shows the drop meshing at $t = 278$, when the drop is well in the throat; the characteristic dimples formed by the solid particles and high mesh quality are demonstrated. As the drop leaves the constriction, it starts elongating very fast in the flow of extensional type behind the spheres; for this reason, we were unable, with the present version of the code, to track the process beyond $t = 345$. In part, this shortcoming is due to using the high-order curvature algorithm of Appendix B. With the best paraboloid-spline method (Zinchenko & Davis 2000) instead, the calculation could be made further (at some modest expense of accuracy, however, for the main stage of drop squeezing), still showing drop stretching to length $5.94\widetilde{a}$

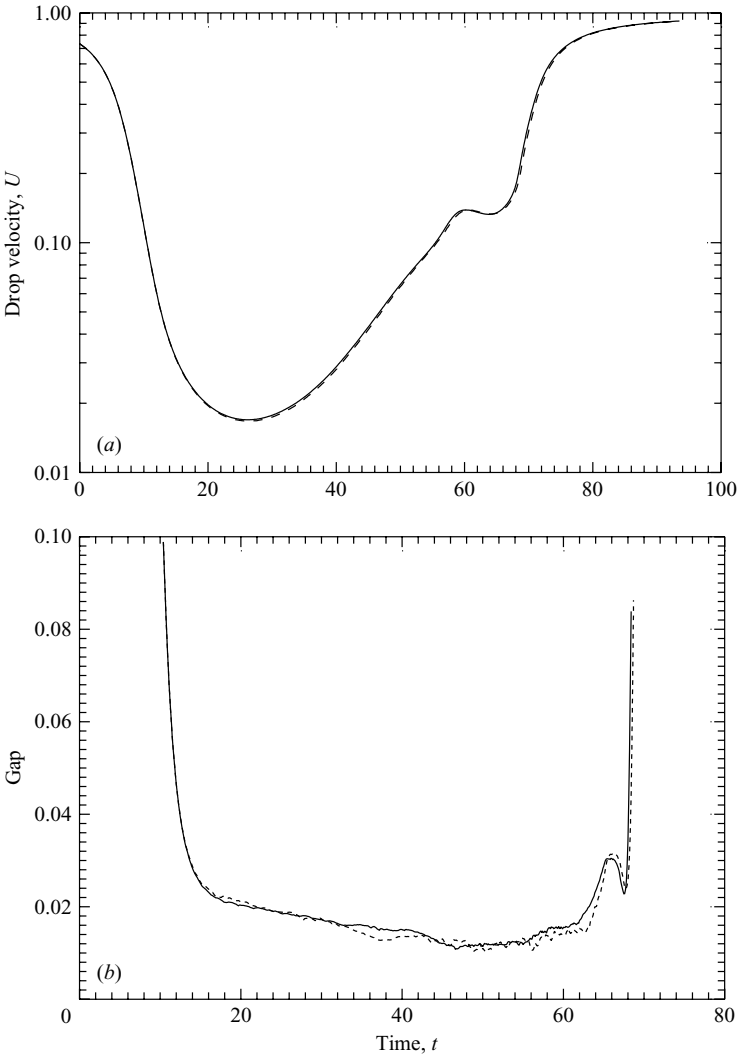

FIGURE 10. (*a*) Drop velocity and (*b*) drop-solid spacing for the motion between two parallel disks ($\varepsilon = 0.5$, $\widetilde{a} = 0.75$, $\lambda = 1$, $Ca = 0.4$). Solid lines: $\widetilde{N}_{\triangle} = 8640$, $\widehat{N}_{\triangle} = 5120$; Dashed lines: $\widetilde{N}_{\triangle} = 5120$, $\widehat{N}_{\triangle} = 3840$.

at $t = 362$, when the drop surface is three units away from the solids. To make such calculations more robust for higher Ca and analyse possible breakup, it would be imperative to either include efficient algorithms of topological mesh restructuring into compact elements (Cristini *et al.* 1998, 2001), or use the curvatureless form of the boundary integral over the drop surface (Zinchenko *et al.* 1999) with fixed-topology meshes. Such potential improvements, however, are outside the scope of the present work, and they may be not even relevant to our future simulations of emulsion flow through a granular material where particles necessarily form a dense packing. Indeed, there will be other solid particles impeding excessive drop elongation as soon as it leaves a constriction; for drops of compact shapes, the present fixed-topology mesh algorithm is quite robust. High-aspect-ratio simulations could be more relevant,

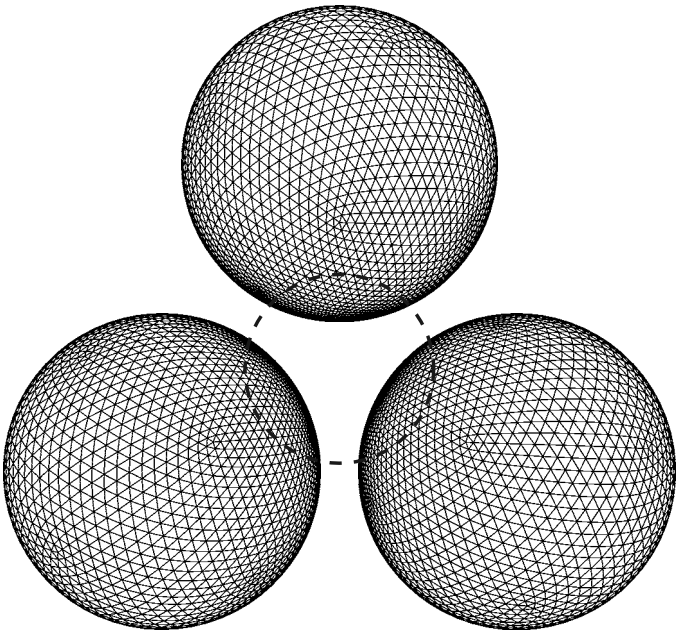

FIGURE 11. A schematic for drop squeezing between three non-touching solid spheres at $\varepsilon = 0.25$, $\widetilde{a} = 0.6$; the mesh of $\widehat{N}_{\triangle} = 5120$ elements on each solid is adapted to the constriction. The projection of the non-deformed drop shape (far upstream) onto the plane of particle centers is shown by the dashed circle.

however, when the non-deformed drop diameter is appreciably smaller than the pore size, if there is a sufficient velocity gradient to stretch/break drops.

The simulation in figure 12 was repeated for several different capillary numbers. In figure 14, the drop velocity U is plotted *vs.* time, the most accurate results (for high resolution) being represented by solid lines. At $Ca = 1.5$, we could only track the simulation to $t \approx 306$ with the high-order curvature scheme, owing to fast drop stretching downstream. By this time, however, the drop is already well out of the constriction, the gap from solid being 0.30. For $Ca = 1.1$, on the other hand, the drop returned to the spherical shape far downstream; at this still supercritical Ca (for squeezing to occur), a dramatic drop deceleration of almost 1000 times in the constriction is observed. The case $Ca = 0.9$ is clearly subcritical: the drop velocity U reaches 10^{-4} by $t = 200$ (and 5×10^{-6} by $t = 600$). The trapped steady state for $Ca = 0.9$ is shown in figure 15, with all normal velocities $\boldsymbol{u} \cdot \boldsymbol{n}$ on the drop surface virtually zero; the drop steady shape is more deformed than in the case of a two-sphere constriction. Figure 16 presents temporal dynamics for the gap between the drop and solids in the $Ca = 0.9$ simulations for high (solid line), moderate (short-dashed line) and low (long-dashed line) resolutions. All runs achieve a true steady state, with the stationary gap of 0.018, 0.015 and 0.013 for low, medium and high resolutions, respectively; the global drop shape in the steady state and trapped configuration (figure 15) were found to be unaffected by these triangulations. Unlike for a two-particle constriction (§ 4.2), the steady state in figures 15 and 16 (with all three gaps between the drop and solids being equal) is asymptotically stable at $t \to \infty$, which was verified by repeating these simulations with slightly asymmetric initial conditions.

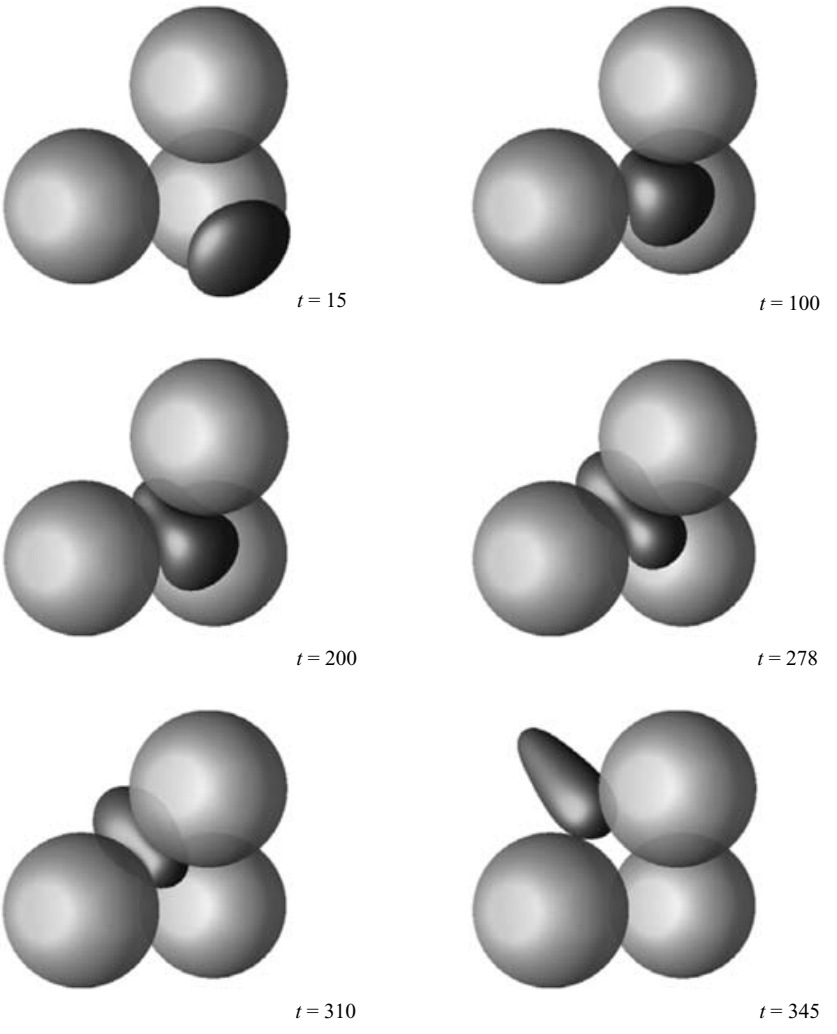

FIGURE 12. Snapshots of the drop motion between three non-touching spheres for $\varepsilon = 0.25$, $\widetilde{a} = 0.6$, $\lambda = 4$, $Ca = 1.3$, $\widetilde{N}_{\triangle} = 8640$ and $\widehat{N}_{\triangle} = 5120$; a perspective view.

We view the ability of our boundary-integral techniques to maintain such a trapped state virtually indefinitely, without a numerical crash, as an essential feature for the success of future simulations of multidrop motion through a random granular material, with many solid particles rigidly held in a periodix box. In such simulations, some drops will move through constrictions, while others, simultaneously, will be trapped at the pore throats, and, for adequate averaging, it will be imperative to be able to maintain the solution for a long time. In this case, 'trapped' does not mean 'stationary', since the exterior of a trapped drop will continue unsteady interaction with the other drops and solids. We found, however, that this vital ability of the algorithm to maintain a trapped state is highly non-trivial and could not be achieved without combining our new desingularization techniques of § 3.1 with Hebeker representation (2.9). With the latter replaced by the Power–Miranda representation (2.7), the $Ca = 0.9$ runs faltered early, with drop-solid overlapping; the low-resolution run ($\widetilde{N}_{\triangle} = 5120$,

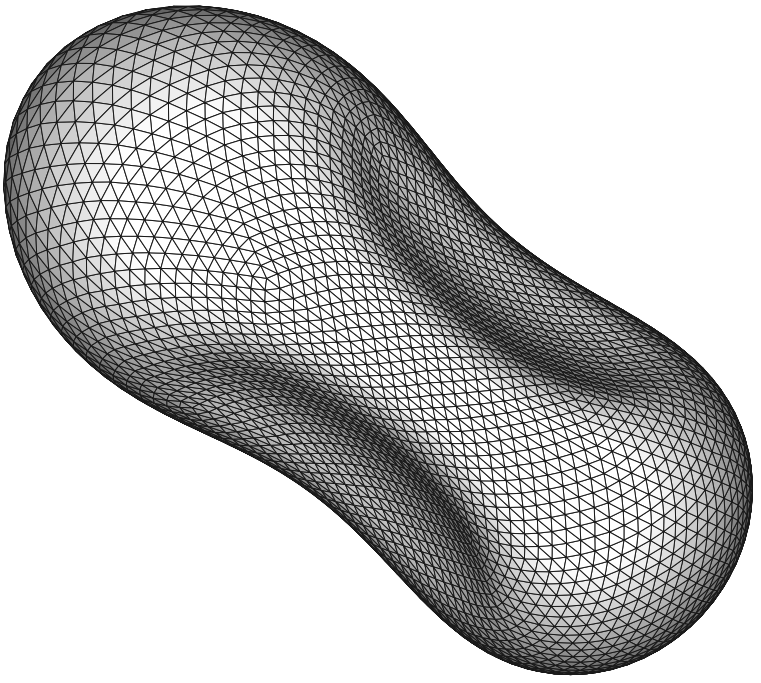

FIGURE 13. Snapshot of the drop meshing at $t = 278$ for squeezing between three non-touching spheres at $\varepsilon = 0.25$, $\widetilde{a} = 0.6$, $\lambda = 4$, $Ca = 1.3$, $\widetilde{N}_{\triangle} = 8640$ and $\widehat{N}_{\triangle} = 5120$; the view direction is perpendicular to $\boldsymbol{u}_{\infty}$ and to the line-of-centres of two of the spheres.

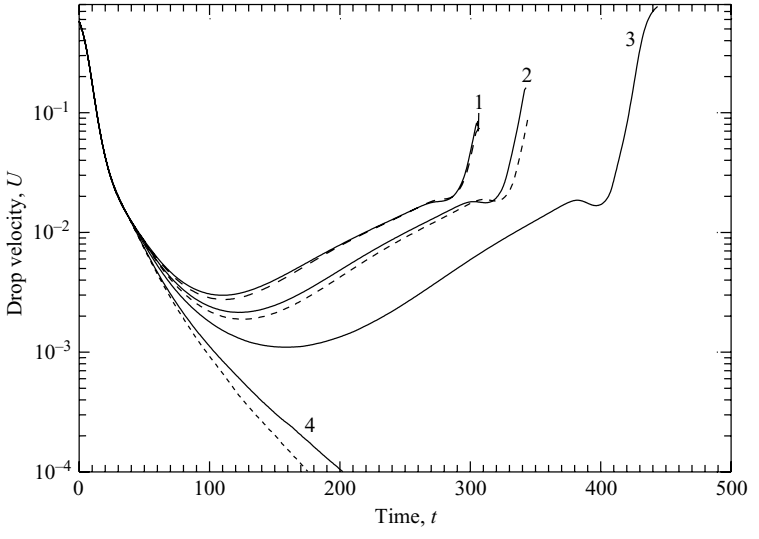

FIGURE 14. Drop velocity for the motion between three non-touching spheres ($\varepsilon = 0.25$, $\widetilde{a} = 0.6$, $\lambda = 4$). Solid lines 1: $Ca = 1.5$; 2: $Ca = 1.3$; 3: $Ca = 1.1$; 4: $Ca = 0.9$, all for $\widetilde{N}_{\triangle} = 11\,520$, $\widehat{N}_{\triangle} = 8640$. Long-dashed ($Ca = 1.5$), medium-dashed ($Ca = 1.3$) and short-dashed ($Ca = 0.9$) lines are for $\widetilde{N}_{\triangle} = 8640$, $\widehat{N}_{\triangle} = 5120$. For essentially supercritical Ca, the triangulation effect is negligible; for $Ca = 0.9$, the drop velocity is practically mesh-independent until it reaches ~ 0.002.

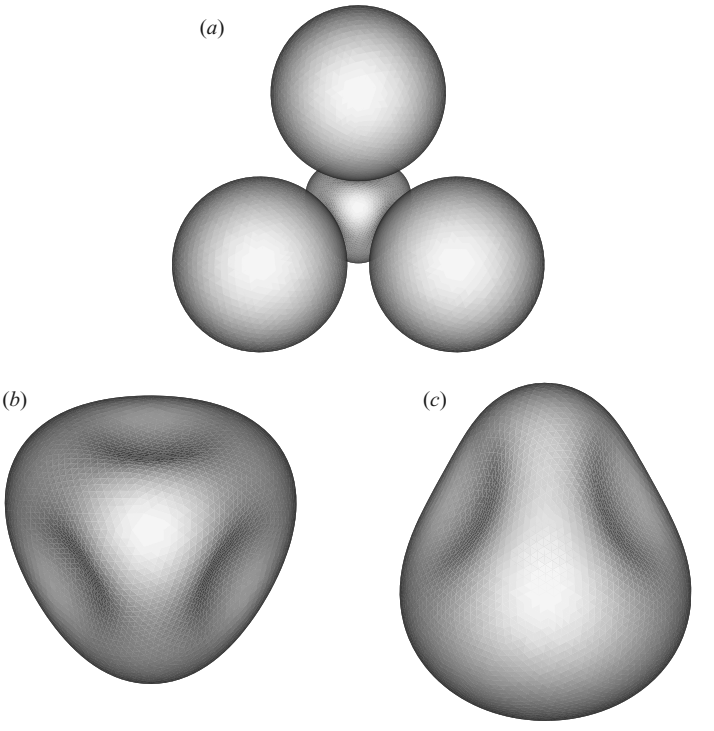

FIGURE 15. (*a*) A trapped configuration and (*b*, *c*) drop steady-state shape between three non touching spheres for $\varepsilon = 0.25$, $\widetilde{a} = 0.6$, $\lambda = 4$, $Ca = 0.9$; (*a*) and (*b*) are front views along $\boldsymbol{u}_\infty$ (with the flow pushing the drop from behind); (*c*) is the side view perpendicular to $\boldsymbol{u}_\infty$ and to the line-of-centres of two of the particles; (*b*) and (*c*) use the same scale.

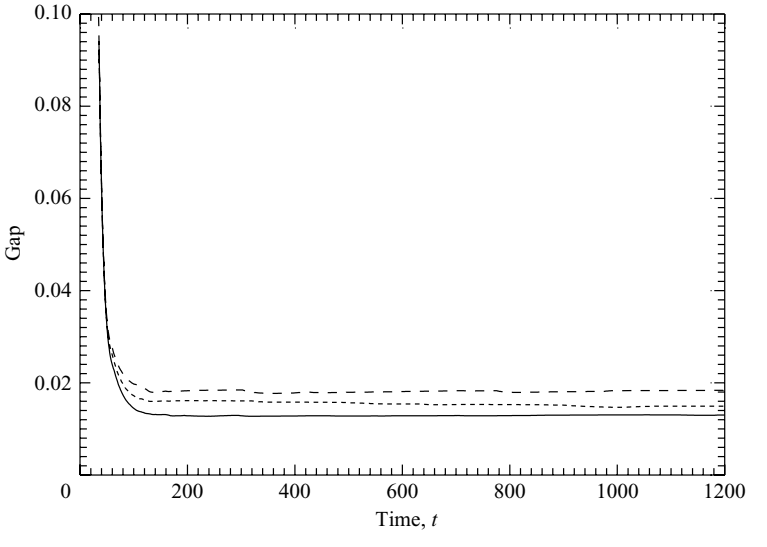

FIGURE 16. The temporal dynamics of the drop-solid spacing for subcritical $Ca = 0.9$ in a three-sphere constriction ($\varepsilon = 0.25$, $\widetilde{a} = 0.6$, $\lambda = 4$). Solid line: $\widetilde{N}_\triangle = 11\,520$, $\widehat{N}_\triangle = 8640$; short-dashed line: $\widetilde{N}_\triangle = 8640$, $\widehat{N}_\triangle = 5120$; long-dashed line: $\widetilde{N}_\triangle = 5120$, $\widehat{N}_\triangle = 3840$.

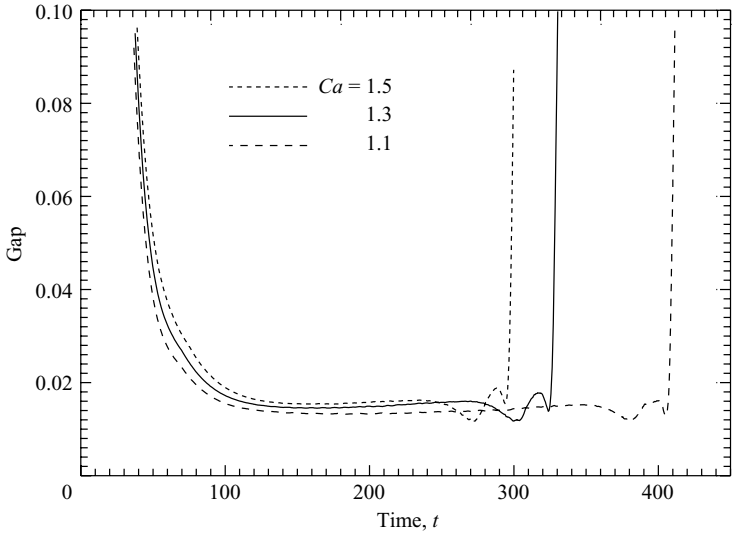

FIGURE 17. Drop–solid spacing for supercritical Ca in a three-sphere constriction ($\varepsilon = 0.25$, $\widetilde{a} = 0.6$, $\lambda = 4$, $\widetilde{N}_{\triangle} = 11\,520$, $\widehat{N}_{\triangle} = 8640$).

$\widehat{N}_{\triangle} = 3840$) crashed at $t = 157$, the medium-resolution run ($\widetilde{N}_{\triangle} = 8640$, $\widehat{N}_{\triangle} = 5120$) could survive only until $t = 167$. For comparison, it takes the drop about twice as long to pass the constriction, even for an essentially supercritical $Ca = 1.5$ (see figure 14). In contrast, with the Hebeker representation, all our runs in igure 16 proceeded to $t = 1600$ and were simply stopped without a sign of failure. Instead of more sophisticated numerical tools offered in the present work, it would seem natural to introduce artificial repulsion forces between the drop and solids to prevent the numerical crash, but so far, we have found this idea to fail: to have a negligible global effect, these forces must be small and they do not help to extend the lifetime of the solution substantially.

It was also interesting to explore the capabilities of the first-kind integral equation in our problem (by disabling the double-layer term in the Hebeker representation (2.9) and forcing the density $\boldsymbol{q}(\boldsymbol{x})$ to be orthogonal to the normal vector $\boldsymbol{n}(\boldsymbol{x})$, to purge the corresponding eigensolutions), since the disadvantages of this generally ill-conditioned tool are sometimes disputed in the literature. It was observed in the $Ca = 1.3$ runs that the number of iterations per time step becomes reasonable (of the order of ten) after a short initial time, thus allowing simulations to proceed despite ill-conditioning, but only until the drop comes close to solids. In the latter case, the number of iterations grew catastrophically, to $O(100)$ and more, especially for larger $\widehat{N}_{\triangle}$, so that high triangulations on solids could not even be attempted. Since the difficulty arises from drop–solid interactions, it could not be resolved by preconditioning on the level of single particles; non-iterative techniques are not prospective at all in this, and especially future large-scale problems. The run $\widetilde{N}_{\triangle} = 8640$, $\widehat{N}_{\triangle} = 1280$ crashed very early at $t = 87$ with drop–solid overlapping; the run $\widetilde{N}_{\triangle} = 8640$, $\widehat{N}_{\triangle} = 2160$ succeeded only to $t = 93$. The first-kind integral equation is far from a suitable approach in the present problem even for $Ca > Ca_{crit}$, let alone for the more difficult subcritical case.

To complement the results in figure 16, we have also calculated the dynamics of the drop–solid clearance for $Ca > C_{crit}$. The high-resolution results in figure 17 reveal, again, that the gap is a surprisingly weak function of Ca in the supercritical range.

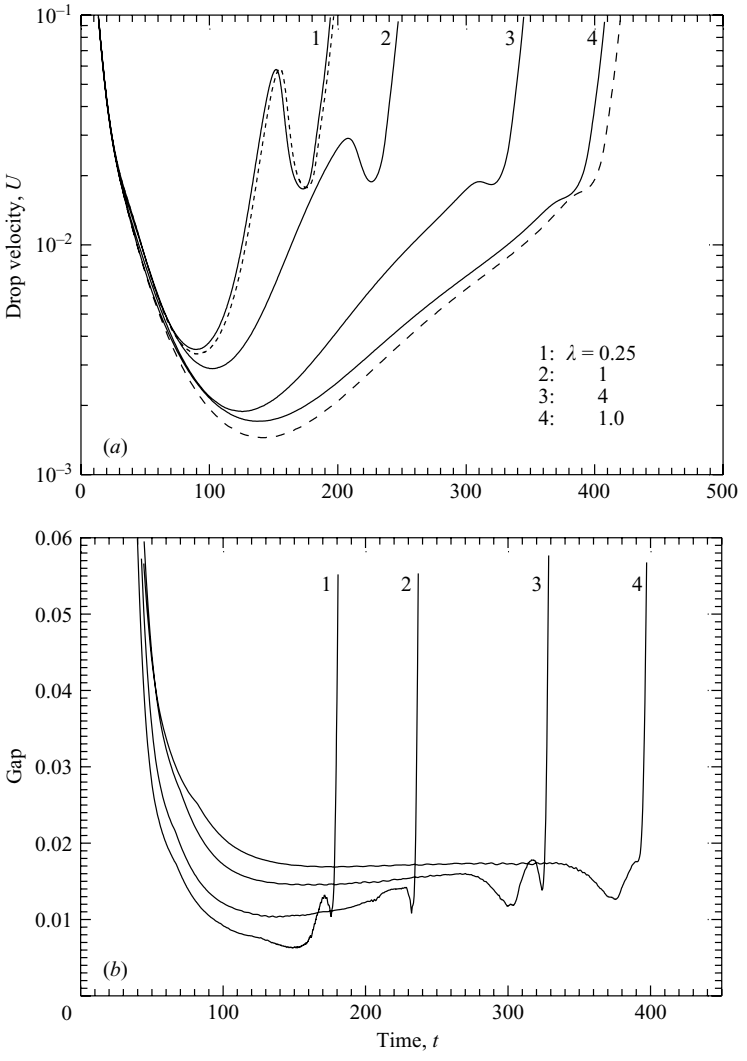

FIGURE 18. The effect of λ on (*a*) the drop velocity and (*b*) drop-solid spacing for squeezing between three non-touching spheres ($\varepsilon = 0.25$, $\tilde{a} = 0.6$, $Ca = 1.3$). Solid lines 1–4 are for $\widetilde{N}_{\triangle} = 11\,520$, $\widehat{N}_{\triangle} = 8640$. Short-dashed ($\lambda = 0.25$) and long-dashed ($\lambda = 10$) lines in (*a*) are for medium resolution $\widetilde{N}_{\triangle} = 8640$, $\widehat{N}_{\triangle} = 5120$.

Even for an essentially supercritical $Ca = 1.5$, the drop has to nearly coat the solid surfaces, with the gap less than ≈ 0.015, to be able to squeeze through the hole.

Figures 18(*a*, *b*) demonstrate the effect of the drop-to-medium viscosity ratio λ on the squeezing process at $Ca = 1.3$. Decreasing λ from 10 to 0.25 shortens the exit time (roughly, the time after which both the drop velocity and drop–solid spacing start to increase sharply) about 2.4 times, obviously due to reduced lubrication. The drop-solid spacing during squeezing is also smaller for $\lambda = 0.25$, reaching 0.006 (figure 18*b*). Since $\lambda = 0.25$ is away from critical, the global triangulation effect is very weak for this λ (cf. short-dashed and solid lines in figure 18*a*), and the exit time is predicted accurately (on the other hand, the small gaps for $\lambda = 0.25$ did not allow the low-resolution run $\widetilde{N}_{\triangle} = 5120$, $\widehat{N}_{\triangle} = 3840$ to succeed at all beyond $t = 102$). For $\lambda = 10$,

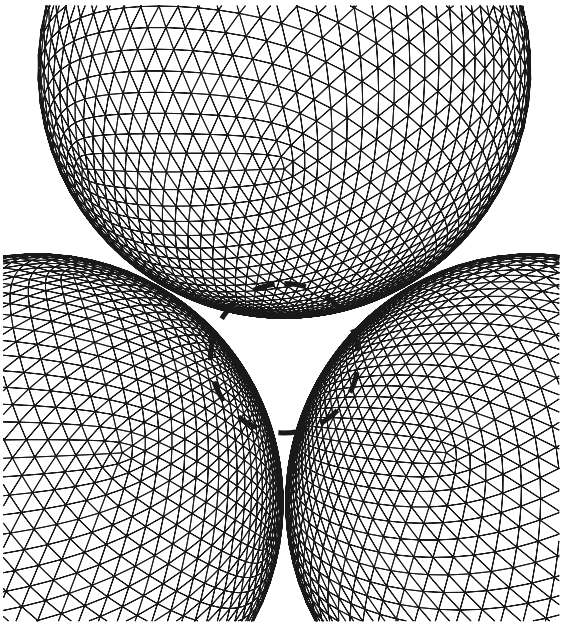

FIGURE 19. A schematic for drop squeezing between three nearly touching solid spheres at $\varepsilon = 0.01$, $\widetilde{a} = 0.3$; the constriction-adaptive mesh on solids with $\widehat{N}_{\triangle} = 5120$ and the projection of the initial non-deformed drop shape (dashed circle) on the plane of particle centers are shown; the drop centre is initially six units away from this plane.

the triangulation effect is the strongest (cf. long-dashed and solid lines in figure 18*a*), but still acceptable; the exit times for high and medium resolutions differ by 4 %.

Finally, we carried out a more difficult series of simulations for drop squeezing between three (nearly) touching solid spheres, which is most relevant to emulsion flow through a packed granular material. The gap $\varepsilon = 0.01$ between solid spheres is made non-zero just to alleviate calculation difficulties due to a touching singularity, without a significant effect on the squeezing process. The non-deformed drop radius is now $\widetilde{a} = 0.3$, which is still about twice as large as the inner radius of the constriction. The stationary adaptive meshes on solids (Appendix C) are quite non-uniform, the maximum-to-minimum mesh edge ratio being about 5 (figure 19). The snapshots of drop squeezing for $\lambda = 4$, $Ca = 1.2$ and high resolution are shown in figure 20. Figure 21(*a*) presents the drop velocity $U(t)$ for $\lambda = 4$ and different capillary numbers. For $Ca = 2$, fast drop stretching is observed far downstream, presumably leading to breakup, while for $Ca = 1.2$ and 1.05, the drop slowly returns to spherical shape after passing through the constriction. The case $Ca = 1$ is obviously near-critical: the drop velocity decelerates to $\approx 10^{-4}$ by $t \approx 600$ before starting to recover; it takes the drop a long time, $t \approx 1300$, to squeeze through (not shown). Figure 21(*b*) shows the dynamics of the drop–solid surface clearance for supercritical Ca; at $Ca = 1.05$–1.2, the gap remains about 0.008–0.009 for the entire squeezing process. The temporal dynamics of drop motion through the constriction for near-critical conditions is inevitably sensitive to triangulations. The critical capillary number, nevertheless, can be determined with acceptable accuracy. Figure 21(*a*) suggests $Ca_{crit} \approx 1$ for high resolution; for medium resolution ($\widetilde{N}_{\triangle} = 8640$, $\widehat{N}_{\triangle} = 5120$), we found it to be between 1.1 (when $U(t)$ reaches 2×10^{-5} by $t = 2000$) and 1.15.

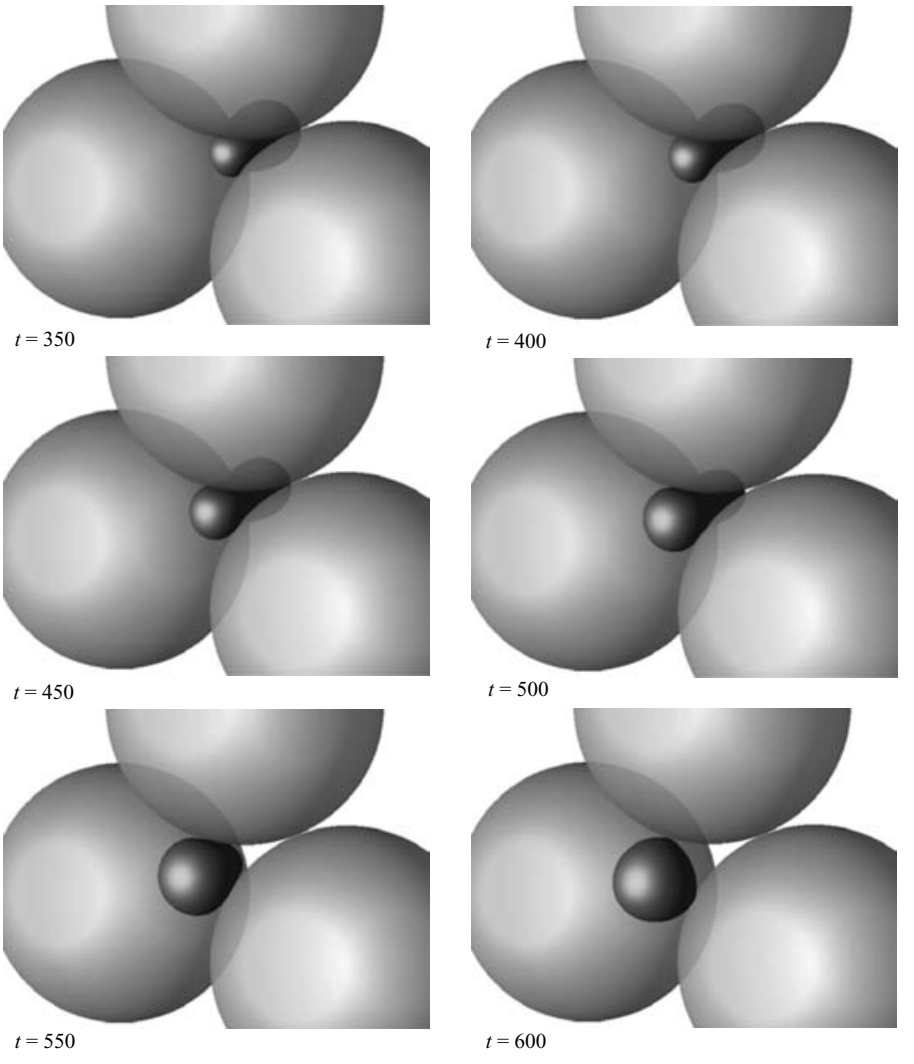

FIGURE 20. Snapshots of the drop motion between three nearly-touching spheres for $\varepsilon = 0.01$, $\widetilde{a} = 0.3$, $\lambda = 4$, $Ca = 1.2$, $\widetilde{N}_{\triangle} = 11\,520$, $\widehat{N}_{\triangle} = 8640$; a perspective view.

In addition to using the Power–Miranda representation (2.7) instead of the Hebeker representation, another modification to the code we have attempted was to use the areas of geodesic triangles on solids instead of flat triangles in (3.2). Both modifications generally improve the accuracy for $Ca > Ca_{crit}$, but, very unfortunately, they make the code fail early for subcritical conditions. The present version of the algorithm for drop squeezing through interparticle constrictions described in §§ 2–3 is recommended as the most balanced approach, which has an acceptable (typically, good) accuracy for $Ca > Ca_{crit}$ and does not lose robustness in the subcritical range.

5. Conclusions

A novel three-dimensional boundary-integral algorithm has been developed to study, for the first time, squeezing of a deformable drop at low Reynolds number

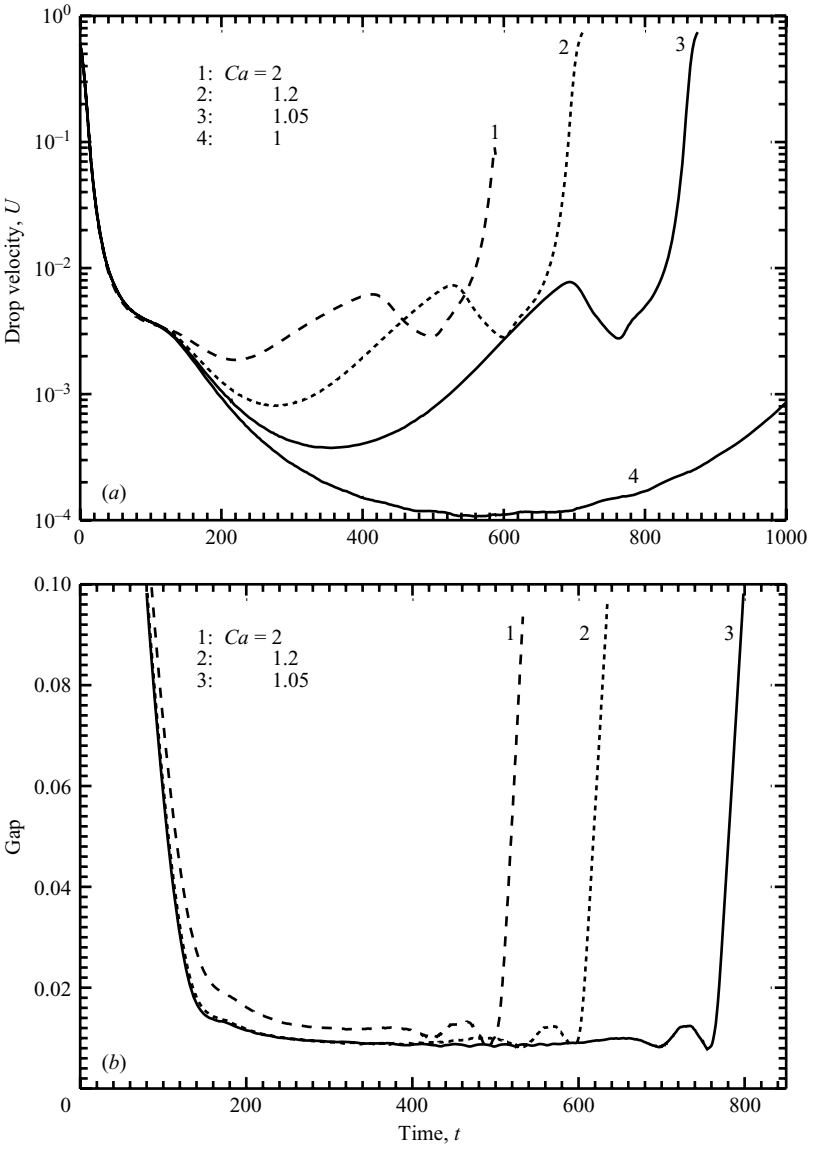

FIGURE 21. (*a*) The drop velocity and (*b*) drop–solid spacing for squeezing between three nearly touching spheres ($\varepsilon = 0.01$, $\tilde{a} = 0.3$, $\lambda = 4$). Medium resolution ($\widetilde{N}_{\triangle} = 8640$, $\widehat{N}_{\triangle} = 5120$) for $Ca = 2$, high resolution ($\widetilde{N}_{\triangle} = 11\,520$, $\widetilde{N}_{\triangle} = 8640$) for other Ca.

through a tight constriction formed by several solid particles rigidly held in space. The drop is freely suspended and driven by a flow which is uniform away from the solid obstacles. This problem serves as a prototype of interactions that would occur for emulsion flow through a random granular material; it is most interesting to determine when (and how fast) the drop can squeeze through, and when it will be trapped in the throat. The study of this prototype problem not only allowed us to clarify the salient features of the emulsion filtration process, but also to develop and test numerical tools that will be suitable in future, much more complex simulations of multidrop motion past a random array of solid obstacles. Realistic emulsion flow

simulations would require periodic boundaries for determining the pressure gradient–flow rate relationship. However, we have chosen here to consider solid particles in an unbounded medium as the first step, to concentrate on principal features of the squeezing mechanism and drop–solid close interaction, and on the related numerical issues not distracted by the details of the periodic boundary implementation. Although the present problem is relatively small-scale (one drop interacting with two or three solid particles), the big challenge for tight constrictions (with the inner diameter several times smaller than the non-deformed drop diameter), and especially for near-critical conditions, is that the drop moves with high resistance and very small clearance, nearly coating the solid obstacles; the subcritical case, when the drop is trapped, is even harder to simulate.

Compared to drop–drop interactions at finite deformations (Loewenberg & Hinch 1996, 1997; Zinchenko *et al.* 1997, 1999; Zinchenko & Davis 2000, 2002, 2003; Bazhlekov *et al.* 2004), the solution for drop–solid interactions is much more lubrication sensitive, and has required advanced numerical techniques to succeed. Our algorithm is based on Hebeker representation for solid–particle contributions (as a proportional combination of single- and double-layer potentials) and new desingularization methods for boundary integrals. The most crucial and promising advance is the high-order near-singularity subtraction in the solid–drop double-layer contribution that we developed; without this element, none of the simulations could succeed. The algorithm also features fixed-topology drop surface triangulations maintained by 'passive mesh stabilization'. The resulting system of second-kind integral equations for the Hebeker density on the solid surfaces and fluid velocity on the drop interface is not suitable for traditional solution by 'successive substitutions', but we have found alternative iterative schemes to succeed. The current version of the code is for spherical and spheroidal (oblate and prolate) solid particles, but generalization to other shapes (e.g. three-dimensional ellipsoids or general axisymmetrical shapes in a three-dimensional configuration) is possible. Even with new numerical tools, the calculations are demanding, requiring 5000–10 000 boundary elements per surface for robustness/accuracy, and typically a few thousand time steps for each run.

Using this algorithm, the drop squeezing between (i) two close spheres and (ii) two parallel disks, and (iii) through the hole between three close spheres forming an equilateral triangle (including the case of very close contact) was simulated for arbitrary viscosity ratios λ. For a two-particle constriction, the drop squeezes in an interesting fashion, with 'collar' formation for $Ca > Ca_{crit}$, and is trapped (wedged) for $Ca < Ca_{crit}$, but the trapped steady state is not asymptotically stable at $t \to \infty$. In contrast, for a three-sphere constriction, the trapped state (for $Ca < Ca_{crit}$) is asymptotically stable. The effect of the constriction type, capillary number and viscosity ratio λ on the drop velocity in the throat, exit time from the constriction, and the drop–solid spacing is explored in detail. Calculations are presented in a challenging range of parameter values, with initial (non-deformed) drop diameter much larger than the inner constriction diameter, and conditions not far from critical; in some simulations, the drop decelerates up to 10^3–10^4 times in the throat, but is still able to pass through. In all cases, the drop–solid surface clearance during squeezing is 0.6 %–2 % of the particle radius (or major half-axis), and is a surprisingly weak function of the capillary number; even for essentially supercritical Ca, the drop has to nearly coat the solid surfaces with small clearance, to be able to squeeze through a tight constriction. For a fixed ratio of the drop non-deformed diameter to the inner constriction diameter, the critical capillary number is only weakly sensitive to

solid–solid spacing in a three-sphere constriction. Increasing λ from 0.25 to 10 has a moderate effect to delay the exit time, and to increase the drop–solid spacing during squeezing, owing to higher lubrication. The numerical convergence is good, except for conditions very close to critical where the temporal dynamics is inevitably sensitive to triangulations. Despite this difficulty, the critical capillary numbers (for squeezing to occur) are predicted reliably.

Presumably, there is a qualitative analogy between the trapped steady states found here for two-sphere and three-sphere constrictions, and the stationary axisymmetrical solutions for a deformable drop near a plane wall and for two drops pressed together by a compressional flow (Nemer 2003; Nemer *et al.* 2004). In all the cases, the steady state with small but non-zero gap thickness is due to the local pumping flow along the drop surface which drives the fluid into the gap(s) to balance the squeezing effect of the outer flow. Nemer *et al.* (2004) showed, however, that for gravity-induced head-on approach of two unequal drops, pumping acts in the opposite direction and leads to exponential film drainage to arbitrarily small thickness. In this connection, it would be very interesting in future work to study the effects of gravitational forcing on drop squeezing through interparticle constrictions and especially on the trapping mechanism.

The ability of our three-dimensional algorithm to maintain a trapped state virtually indefinitely without a numerical crash (at least, for conditions not too close to critical) was found to be highly non-trivial and could not be achieved without combining our new desingularization tools with the Hebeker representation. This feature is expected to be very important for the success of future simulations of multidrop motion through a random packed granular material, with many solid particles rigidly held in a periodic box. Indeed, in such simulations, some drops will move through interparticle constrictictions, while others, simultaneously, will be trapped at the pore throats and, for adequate averaging, it will be imperative to be able to maintain the solution for long times. In future work, we hope to address such very challenging simulations by combining the present boundary-integral tools with efficient multipole acceleration techniques (Zinchenko & Davis 2000, 2002, 2003), methods for simulating granular microstructures (Zinchenko 1994, 1998), and parallel programming. An appropriate choice between the 'constant flow rate' and 'constant pressure gradient' formulations may be an additional issue in such simulations and is not obvious a *priori*. For drop motion in periodically constricted tubes, the distinction between the two formulations is analysed by Graham & Higdon (2000*b*).

This work was supported by NASA grant NNCO5GA55G, and by grant 40430-AC from the Petroleum Research Fund of the American Chemical Society.

Appendix A. Analytical calculation of singular and near-singular integrals over a solid particle

General formulae. Using the Gauss theorem, we have for an arbitrarily shaped particle $\widehat{S}_\beta$ and $\boldsymbol{y}$ outside $\widehat{S}_\beta$:

$$\int_{\widehat{S}_\beta}\left(\frac{\delta_{ij}}{r}+\frac{r_i r_j}{r^3}\right)\mathrm{d}S_{\boldsymbol{x}}=(\delta_{ij}-R_i\nabla_j)\int_{\widehat{S}_\beta}\frac{\mathrm{d}S_{\boldsymbol{x}}}{r}+\nabla_j\int_{\widehat{S}_\beta}\frac{\xi_i}{r}\,\mathrm{d}S_{\boldsymbol{x}}, \tag{A 1}$$

with $\nabla_j=\partial/\partial y_j$, $\boldsymbol{\xi}=\boldsymbol{x}-\widehat{\boldsymbol{x}}^c_\beta$, and $\boldsymbol{R}=\boldsymbol{y}-\widehat{\boldsymbol{x}}^c_\beta$, which reduces the calculation of the Green function integrals (3.4) to surface Newtonian potentials with constant and linear densities.

To prove (3.16) for an arbitrary shape, we again use the Gauss theorem

$$\Psi_{k,\ell,m} = \int_{\widehat{\mathscr{D}}_\beta} \tau_{k,\ell,m}(\boldsymbol{r})\,\mathrm{d}V_{\boldsymbol{x}} = \int_{\widehat{\mathscr{D}}_\beta} \left[-p^k\delta_{\ell m} + \frac{\partial G_{k\ell}}{\partial x_m} + \frac{\partial G_{km}}{\partial x_\ell}\right] \mathrm{d}V_{\boldsymbol{x}}, \tag{A 2}$$

where $p^k = (4\pi)^{-1}\partial(r^{-1})/\partial x_k$ is the fundamental pressure for the Green function (2.2). Note that

$$\int_{\widehat{\mathscr{D}}_\beta} \frac{\partial G_{k\ell}}{\partial x_m}\,\mathrm{d}V_{\boldsymbol{x}} = \frac{1}{8\pi}\nabla_m \int_{\widehat{\mathscr{D}}_\beta} \left[\frac{\delta_{k\ell}}{r} + (\xi_\ell - R_\ell)\nabla_k\left(\frac{1}{r}\right)\right] \mathrm{d}V_{\boldsymbol{x}}. \tag{A 3}$$

Substituting (A 3) and a similar relation for $\partial G_{km}/\partial x_\ell$ into (A 2) yields (3.16), after some algebra.

Spherical particle. In this case, the homogeneous Newtonian potentials are standard:

$$\int_{\widehat{S}_\beta} \frac{\mathrm{d}S_{\boldsymbol{x}}}{r} = \frac{4\pi a_\beta^2}{R}, \quad \int_{\widehat{\mathscr{D}}_\beta} \frac{\mathrm{d}V_{\boldsymbol{x}}}{r} = \frac{4}{3}\,\frac{\pi a_\beta^3}{R} \quad (R \geqslant a_\beta). \tag{A 4}$$

For a linear density $\boldsymbol{\xi}$, it is easy to derive

$$\int_{\widehat{\mathscr{D}}_\beta} \frac{\boldsymbol{\xi}}{r}\,\mathrm{d}S_{\boldsymbol{x}} = \tfrac{4}{3}\pi a_\beta^4 \frac{\boldsymbol{R}}{R^3}, \quad \int_{\widehat{\mathscr{D}}_\beta} \frac{\boldsymbol{\xi}}{r}\,\mathrm{d}V_{\boldsymbol{x}} = \tfrac{4}{15}\pi a_\beta^5 \frac{\boldsymbol{R}}{R^3}. \tag{A 5}$$

Substituting (A 4)–(A 5) into (A 1) and (3.16), yields (3.4) and (3.17) after some straightforward operations.

Prolate spheroid. Let (ρ, z) be cylindrical coordinates with the origin at the particle centre and the z-axis along the particle axis of symmetry. The prolate spheroidal coordinates σ, τ are introduced as (Korn & Korn 1968)

$$\rho = c(\sigma^2 - 1)^{1/2}(1 - \tau^2)^{1/2}, \quad z = c\sigma\tau, \quad \sigma > 1, \quad -1 \leqslant \tau \leqslant 1. \tag{A 6}$$

A given particle $\widehat{S}_\beta$ becomes a coordinate surface $\sigma = \sigma_0 =$ const, if $\sigma_o = p/(p^2 - 1)^{1/2}$ and $c = (a^2 - b^2)^{1/2}$, where a, b are half-axes ($a > b$), and $p = a/b$ is the aspect ratio.

To expand the surface potentials (A 1) in spheroidal harmonics, we start from the relation

$$\left(\sigma_o^2 - \tau^2\right)^{1/2} = \sigma_o\left[1 - \sum_{n=0}^{\infty} P_{2n}(\tau) \sum_{k=\max(1,n)}^{\infty} \frac{(2k-3)!!\,(2k-1)!!\,2^{n-k}(4n+1)}{\sigma_o^{2k}(k-n)!(2k+2n+1)!!}\right], \tag{A 7}$$

where $P_m(\tau)$ is a standard Legendre polynomial of degree m. Equation (A 7) can be briefly written as

$$\left(\sigma_o^2 - \tau^2\right)^{1/2} = \sum_{n=0}^{\infty} K_n P_{2n}(\tau), \tag{A 8}$$

and allows us to compute the coefficients K_n. Based on (A 8), it can be shown that for $\boldsymbol{y}$ outside $\widehat{S}_\beta$

$$\int_{\widehat{S}_\beta} \frac{\mathrm{d}S_{\boldsymbol{x}}}{r} = 4\pi c\left(\sigma_o^2 - 1\right)^{1/2} \sum_{n=0}^{\infty} K_n \mathscr{B}_{2n}(\sigma_o)\mathscr{D}_{2n}(\sigma)P_{2n}(\tau),$$

$$\int_{\widehat{S}_\beta} \frac{\boldsymbol{\xi}}{r}\,\mathrm{d}S_{\boldsymbol{x}} = \sum_{n=1,3,\ldots} F_n \mathscr{D}_n(\sigma)P_n(\tau)\boldsymbol{d} + [\boldsymbol{R} - (\boldsymbol{R}\cdot\boldsymbol{d})\boldsymbol{d}] \sum_{n=1,3,\ldots} E_n \mathscr{D}_n'(\sigma)P_n'(\tau), \tag{A 9}$$

with

$$E_{2n+1} = \frac{4\pi c\left(\sigma_o^2-1\right)^{3/2}\mathscr{B}'_{2n+1}(\sigma_o)}{(2n+1)(2n+2)}\left[\frac{K_{n+1}}{4n+5}-\frac{K_n}{4n+1}\right],$$

$$F_{2n+1} = 4\pi c^2\sigma_o\left(\sigma_o^2-1\right)^{1/2}\mathscr{B}_{2n+1}(\sigma_o)\left[\frac{2n+1}{4n+1}K_n+\frac{2n+2}{4n+5}K_{n+1}\right]. \tag{A 10}$$

Here, $\boldsymbol{d}$ is the unit director of the particle (z) axis, $\mathscr{B}_n(\sigma)$ is simply $P_n(\sigma)$, defined in the range $\sigma > 1$, and $\mathscr{D}_n(\sigma)$ is the Legendre function of the second kind

$$\mathscr{D}_n(\sigma) = \frac{1}{2}\int_{-1}^{1}\frac{P_n(t)\,\mathrm{d}t}{\sigma-t} = \sum_{k=0}^{\infty}\frac{2^{n+1}(2k-1)!!}{(2k+2n+1)!!}\,\frac{(n+k)!}{k!(\sigma+\sqrt{\sigma^2-1})^{n+1+2k}}. \tag{A 11}$$

Substituting the exterior potentials (A 9) into (A 1), the infinite sums are differentiated as compound functions of $\boldsymbol{y}$, with $\sigma = (R_1+R_2)/(2c)$ and $\tau = (R_2-R_1)/(2c)$ taken into account, where R_1 and R_2 are the distances from $\boldsymbol{y}$ to the spheriod foci. The convergence is fast, even in the most unfavourable case $\boldsymbol{y} \in \widehat{S}_\beta$ ($\sigma = \sigma_o$), at least for moderate aspect ratios (we tested $a/b = 2.5$), so 20–30 terms in each sum (A 9) suffice for high accuracy. Fast and stable calculations of $\mathscr{D}_n(\sigma)$ and $\mathscr{B}_n(\sigma)$ at large n are based on the Thomas algorithm for tridiagonal systems via recurrent relations; derivatives are calculated by additional recurrent relations in the order of ascending n.

Calculation of the the volume potentials in (3.16) is simpler, since no infinite expansions are involved:

$$\int_{\widehat{\mathscr{D}}_\beta}\frac{\boldsymbol{\xi}\,\mathrm{d}V_{\boldsymbol{x}}}{r} = [f_1\mathscr{D}_1(\sigma)P_1(\tau)+f_3\mathscr{D}_3(\sigma)P_3(\tau)]\boldsymbol{d}+[e_1\mathscr{D}'_1(\sigma)+e_3\mathscr{D}'_3(\sigma)P'_3(\sigma)][\boldsymbol{R}-(\boldsymbol{R}\cdot\boldsymbol{d})\boldsymbol{d}],$$

$$\int_{\widehat{\mathscr{D}}_\beta}\frac{1}{r}\,\mathrm{d}V_{\boldsymbol{x}} = \tfrac{4}{3}\pi c^2\sigma_o\left(\sigma_o^2-1\right)[\mathscr{D}_o(\sigma)P_o-\mathscr{D}_2(\sigma)P_2(\tau)], \tag{A 12}$$

where

$$\begin{aligned} e_1 &= -\tfrac{2}{5}\pi c^2\sigma_o\left(\sigma_o^2-1\right)^2, \qquad & e_3 &= \frac{\pi}{15}c^2\sigma_o\left(\sigma_o^2-1\right)^2,\\ f_1 &= \tfrac{4}{5}\pi c^3\sigma_o^3\left(\sigma_o^2-1\right), & f_3 &= -f_1. \end{aligned} \tag{A 13}$$

The simplest way of deriving (A 9)–(A 10), (A 12)–(A 13) is based on the jump properties of the Newtonian surface and volume potentials, and on the Wronskian form (Morse & Feshbach 1953) for Legendre functions; details are available upon request from the authors. Equation (A 12) is equivalent to that derived in the classical potential theory (MacMillan 1930).

Oblate spheroids. In this case, the first equation (A 6) is replaced by $\rho = c(1+\sigma^2)^{1/2}(1-\tau^2)^{1/2}$, and the spheroidal coordinate σ is in the range $\sigma \geqslant 0$. The surface $\widehat{S}_\beta$ becomes a coordinate surface $\sigma = \sigma_o = $ const, if $\sigma_o = (p^2-1)^{-1/2}$ and $c = (a^2-b^2)^{1/2}$, where $p = a/b > 1$ is the aspect ratio. The generating expansions (A 7)–(A 8) are replaced by

$$\left(\sigma_o^2+\tau^2\right)^{1/2} = \sum_{n=0}^{\infty}K_nP_{2n}(\tau)$$

$$= \left(\sigma_o^2+1\right)^{1/2}\left[1-\sum_{n=0}^{\infty}P_{2n}(\tau)\sum_{k=\max(1,n)}^{\infty}\frac{(2k-3)!!(4n+1)(-1)^nk!(2n-1)!!}{\left(\sigma_o^2+1\right)^k(k-n)!n!(2k+2n+1)!!}\right]. \tag{A 14}$$

Instead of $\mathscr{D}_n$ and $\mathscr{B}_n$, we introduce real functions

$$\mathscr{O}_n(\sigma) = i^{n+1}\mathscr{D}_n(i\sigma) = \sum_{k=0}^{\infty} \frac{2^{n+1}(2k-1)!!(-1)^k(n+k)!}{(2k+2n+1)!!\,k!(\sigma+\sqrt{\sigma^2+1})^{n+1+2k}}, \tag{A 15}$$

and $\mathscr{W}_n(\sigma) = (-i)^n P_n(i\sigma)$. With the coefficients K_n now determined from (A 14), all the relations (A 9)–(A 10), (A 12) hold for the oblate spheroid case, if $\mathscr{D}_n(\mathscr{B}_n)$ is replaced by $\mathscr{O}_n(\mathscr{W}_n)$, and $\sigma_o^2 - 1$ replaced by $\sigma_o^2 + 1$, except that there should be a plus sign in the square brackets of (A 12). Equations (A 13) are replaced by

$$\left.\begin{aligned} e_1 &= -\tfrac{2}{5}\pi c^2\sigma_o\left(\sigma_o^2+1\right)^2, \quad e_3 = -\frac{\pi}{15}c^2\sigma_o\left(\sigma_o^2+1\right)^2, \\ f_1 &= \tfrac{4}{5}\pi c^3\sigma_o^3\left(\sigma_o^2+1\right), \qquad f_3 = f_1. \end{aligned}\right\} \tag{A 16}$$

The coordinates σ, τ are now given by

$$\sigma^2 = \frac{1}{2}\left\{\frac{R^2}{c^2} - 1 + \left[\left(\frac{R^2}{c^2}-1\right)^2 + \frac{4(\boldsymbol{R}\cdot\boldsymbol{d})^2}{c^2}\right]^{1/2}\right\}, \quad \tau = \frac{\boldsymbol{R}\cdot\boldsymbol{d}}{c\sigma}, \tag{A 17}$$

which are also used to differentiate the external potentials (A 9) and (A 12) as compound functions of $\boldsymbol{y}$. Fast and stable calculations of $\mathscr{O}_n(\sigma)$ and $\mathscr{W}_n(\sigma)$ and their derivatives at large n are necessarily different from those for $\mathscr{D}_n(\sigma)$ and $\mathscr{B}_n(\sigma)$. They are now based on recurrent relations for $\mathscr{W}_n(\sigma)$ in ascending order, and for $\mathscr{O}_n(\sigma)$ in descending order of n.

Appendix B. High-order curvature and normal vector calculations

Let $\boldsymbol{n}_o(\boldsymbol{x}^i)$ be a sufficiently good approximation to $\boldsymbol{n}(\boldsymbol{x}^i)$, and $(x',\ y',\ z')$ be local (intrinsic) Cartesian coordinates centred at $\boldsymbol{x}^i$ and with the z'-axis along $\boldsymbol{n}_o(\boldsymbol{x}^i)$. In these coordinates, the drop surface near $\boldsymbol{x}^i$ is approximated as

$$\begin{aligned} z' \approx R_4(x',\ y') = {} & Ax' + By' + Cx'^2 + Dx'y' + Ey'^2 \\ & + \{x'^3,\ x'^2y,\ x'y'^2,\ y'^3,\ x'^4,\ x'^3y',\ x'^2y'^2,\ x'y'^3,\ y'^4\}, \end{aligned} \tag{B 1}$$

where $\{\ldots\}$ is a combination of third- and fourth-order terms with arbitrary coefficients. These coefficients, along with A, B, C, D and E, are found from local least-squares fitting:

$$\sum_{j\in\mathscr{A}_i\cup\mathscr{A}_i^{(2)}} [z'_j - R_4(x'_j,\ y'_j)]^2 \to \min. \tag{B 2}$$

Here, $\mathscr{A}_i$ is the set of mesh nodes directly connected to $\boldsymbol{x}^i$, and $\mathscr{A}_i^{(2)}$ is the second layer of nodes around $\boldsymbol{x}^i$. Since, for the fixed topology meshes we are using, each node has six (minimum five, in rare cases) neighbours, the number of elements in $\mathscr{A}_i \cup \mathscr{A}_i^{(2)}$ is at least 14 (typically 18). Accordingly, the linear (and symmetric) 14×14 system of equations for the coefficients of $R_4(x',\ y')$ obtained from (B 2) is uniquely solvable. With A, B, etc. found, the normal vector $\boldsymbol{n}(\boldsymbol{x}^i)$ is calculated as

$$\boldsymbol{n}(\boldsymbol{x}^i) = (-A,\ -B,\ 1)/(1+A^2+B^2)^{1/2} \tag{B 3}$$

(in intrinsic coordinates), while the mean curvature at $\boldsymbol{x}^i$ takes the form

$$k(\boldsymbol{x}^i) = \frac{-C(1+B^2) - E(1+A^2) + DAB}{(1+A^2+B^2)^{3/2}}. \tag{B 4}$$

This method, although slightly more complex than the best-paraboloid algorithm, remains fast, since no iterations are involved (unlike in Zinchenko *et al.* 1997, we are not trying to reach $A = B = 0$ iteratively). The initial approximations $\boldsymbol{n}_o(\boldsymbol{x}^i)$ were prepared by the best paraboloid-spline method (Zinchenko & Davis 2000), although a simpler choice of the normal vectors from the preceding time step as $\boldsymbol{n}_o$ would probably suffice.

Appendix C. Constriction-adaptive meshing of spherical particles

Let $\boldsymbol{x}_o$ be the constriction centre. An initial, uniform unstructured triangulation on each sphere $\widehat{S}_\alpha$ is modified iteratively to adapt it to the distances from $\boldsymbol{x}_o$. Namely, the new positions of the mesh nodes $\boldsymbol{x}^i$ after an iteration are

$$\boldsymbol{x}^i_{new} = \zeta\ \boldsymbol{x}^{i,o}_{new} + (1-\zeta)\boldsymbol{x}^i, \quad \boldsymbol{x}^{i,o}_{new} = \left(\sum_{j\in\mathscr{A}_i} W_j\right)^{-1} \sum_{j\in\mathscr{A}_i} W_j \boldsymbol{x}_j, \tag{C 1}$$

where $\mathscr{A}_i$ is the set of nodes on $\widehat{S}_\alpha$ directly connected to $\boldsymbol{x}^i$, $W_j = \parallel \boldsymbol{x}^j - \boldsymbol{x}_o \parallel^{-\alpha}$, and $\alpha > 0$ is the adaptation parameter. The relaxation parameter ζ is used for gradual mesh transition

$$\zeta = 0.25\ \min_i\ \frac{\Delta x_i}{\parallel \boldsymbol{x}^{i,o}_{new} - \boldsymbol{x}^i \parallel}, \tag{C 2}$$

where Δx_i is the shortest distance from $\boldsymbol{x}^i$ to its neighbours $\boldsymbol{x}^j$, $j \in \mathscr{A}_i$, and the minimum in (C 2) is taken over all nodes $\boldsymbol{x}^i \in \widehat{S}_\alpha$. After the operations (C 1), nodes $\boldsymbol{x}^i_{new}$ are scaled about the particle centre $\widehat{\boldsymbol{x}}^c_\alpha$ to remain on $\widehat{S}_\alpha$. Let

$$\chi = \max_i(W_i \Delta x_i)/\min_i(W_i \Delta x_i). \tag{C 3}$$

Small values of χ yield adaptivity, the mesh size Δx_i correlating with $\|\boldsymbol{x}^i - \boldsymbol{x}_o\|^\alpha$. Accordingly, we start monitoring the ratio (C 3) after about 10 iterations, and stop calculations when χ reaches a local minimum. The larger α, the higher the adaptivity, but we found only moderately adaptive meshes to be useful in the calculations of § 4, achieved for $\alpha = 1/2$.

This simple, fixed-topology algorithm can be generalized for non-spherical shapes and multiparticle systems.

REFERENCES

Bazhlekov, I. B., Anderson, P. D. & Meijer, H. E. H. 2004 Nonsingular boundary integral method for deformable drops in viscous flows. *Phys. Fluids* **16**, 1064–1081.

Borhan, A. & Hemmat, M. 1997 Deformation of viscous drops in flow through sinusoidally constricted capillaries. In *Moving Boundaries IV Computational Modeling of Free and Moving Boundary Problems* (ed. R. Van Keer & C. A. Brebbia), pp. 275–284. Computational Mechanics.

Cristini, V., Bławzdziewicz, J. & Loewenberg, M. 1998 Drop breakup in three-dimensional viscous flows. *Phys. Fluids* **10**, 1781–1783.

Cristini, V., Bławzdziewicz, J. & Loewenberg, M. 2001 An adaptive mesh algorithm for evolving surfaces: simulations of drop breakup and coalescence. *J. Comput. Phys.* **168**, 445–463.

Cristini, V., Bławzdziewicz, J., Loewenberg, M. & Collins, L. R. 2003 Breakup in stochastic Stokes flows: sub-Kolmogorov drops in isotropic turbulence. *J. Fluid Mech.* **492**, 231–250.

Hemmat, M. & Borhan, A. 1996 Buoyancy-driven motion of drops and bubbles in a periodically constricted capillary. *Chem. Engng Commun.* **148–150**, 363–384.

Graham, D. R. & Higdon, J. J. L. 2000*a* Oscillatory flow of droplets in capillary tubes. Part 1. Straight tubes. *J. Fluid Mech.* **425**, 31–53.

Graham, D. R. & Higdon, J. J. L. 2000*b* Oscillatory flow of droplets in capillary tubes. Part 2. Constricted tubes. *J. Fluid Mech.* **425**, 55–57.

Hebeker, F.-K. 1986 Efficient boundary element methods for three-dimensional exterior viscous flow. *Numer. Meth. PDE* **2**, 273–297.

Kennedy, M. R., Pozrikidis, C. & Skalak, R. 1994 Motion and deformation of liquid drops, and the rheology of dilute emulsions in simple shear flow. *Comput. Fluids* **23**, 251–278.

Kim, S. & Karilla, S. 1991 *Microhydrodynamics: Principles and Selected Applications.* Butterworth–Heinemann, Boston, MA.

Kokal, S. L., Maini, B. B. & Woo, R. 1992 Flow of emulsions in porous media. In *Emulsions Fundamentals and Applications in the Petroleum Industry* (ed. L. L. Schramm), Advances in Chemistry Series, vol. 231.

Korn, G. A. & Korn, T. M. 1968 *Mathematical Handbook for Scientists and Engineers.* McGraw–Hill, New York.

Ladyzhenskaya, O. A. 1969 *The Mathematical Theory of Viscous Incompressible Flow*, 2nd edn. Gordon & Breach.

Leyrat-Maurin, A. & Barthès-Biesel, D. 1994 Motion of a deformable capsule through a hyperbolic constriction. *J. Fluid Mech.* **279**, 135–163.

Loewenberg, M. & Hinch, E. J. 1996 Numerical simulation of a concentrated emulsion in shear flow. *J. Fluid Mech.* **321**, 395–419.

Loewenberg, M. & Hinch, E. J. 1997 Collision of two deformable drops in shear flow. *J. Fluid Mech.* **338**, 299–315.

MacMillan, W. D. 1930 *The Theory of Potential.* McGraw–Hill.

Martinez, M. J. & Udell, K. S. 1988 Axisymmetric creeping motion of drops through a periodically constricted tube. *AIP Conf. Proc.* **197**, 222–234.

Morse, P. & Feshbach, H. 1953 *Methods of Theoretical Physics.* McGraw–Hill.

Mosler, A. B. & Shaqfeh, E. S. G. 1997 Drop breakup in the flow through fixed beds via stochastic simulation in model Gaussian fields. *Phys. Fluids* **9**, 3209–3226.

Nemer, M. 2003 *Near-contact motion of liquid drops in emulsions and foams.* PhD thesis, Yale University, USA.

Nemer, M. B., Chen, X., Papadopoulos, D. H., Bławzdziewicz, J. & Loewenberg, M. 2004 Hindered and enhanced coalescence of drops in Stokes flow. *Phys. Rev. Lett.* **92**, 114501.

Odqvist, F. K. G. 1930 Über die randwertaufgaben der hydrodynamik zäher Flüssigkeiten. *Math. Z.* **32**, 329–375.

Olbricht, W. L. 1996 Pore-scale prototypes of multiphase flow in porous media. *Annu. Rev. Fluid Mech.* **28**, 187–213.

Olbricht, W. L. & Leal, L. G. 1983 The creeping motion of immiscible drops through a converging/diverging tube. *J. Fluid Mech.* **134**, 329–355.

O'Neill, M. E. & Majumdar, S. R. 1970 Asymmetrical slow viscous motions caused by the translation or rotation of two spheres. Part I. The determination of exact solutons for any values of the ratio of radii and separation parameters. *Z Angew. Math. Phys.* **21**, 164–179.

Patel, P. D., Shaqfeh, E. S. G., Butler, J. E., Cristini, V., Bławzdziewicz, J. & Loewenberg, M. 2003 Drop breakup in the flow through fixed fibre beds: an experimental and computational investigation. *Phys. Fluids* **15**, 1146–1157.

Power, H. & Miranda, G. 1987 Second kind integral equation formualtion of Stokes flow past a particle of arbitrary shape. *SIAM J. Appl. Maths* **47**, 689–698.

Pozrikidis, C. 1992 *Boundary Integral and Singularity Methods for Linearized Viscous Flow.* Cambridge University Press.

Pozrikidis, C. 2005 Numerical simulation of cell motion in tube flow. *Ann. Biomed. Engng* **33**, 165–178.

Quéguiner, C. & Barthès-Biesel, D. 1997 Axisymmetric motion of capsules through cylindrical channels. *J. Fluid Mech.* **348**, 349–376.

Rallison, J. M. 1981 A numerical study of the deformation and burst of a viscous drop in general shear flows. *J. Fluid Mech.* **109**, 465–482.

Rallison, J. M. & Acrivos, R. 1978 A numerical study of the deformation and burst of a viscous drop in an extensional flow. *J. Fluid Mech.* **89**, 191–200.

Stimson, M. & Jeffrey, G. B. 1926 The motion of two spheres in a viscous fluid. *Proc. R. Soc. Lond.* A **111**, 110–116.

Tsai, T. M. & Miksis, M. J. 1994 Dynamics of a drop in a constricted capillary tube. *J. Fluid Mech.* **274**, 197–217.

Zinchenko, A. Z. 1983 Calculation of the effectiveness of gravitational coagulation of drops with allowance for internal circulation. *Prikl. Matem. Mekhan.* **46**, 58–65.

Zinchenko, A. Z. 1994 Algorithm for random close packing of spheres with periodic boundary conditions. *J. Comput. Phys.* **114**, 298–307.

Zinchenko, A. Z. 1998 Effective conductivity of loaded granular materials by numerical simulation. *Phil. Trans. R. Soc. Lond.* A **356**, 2953–2998.

Zinchenko, A. Z. & Davis, R. H. 2000 An efficient algorithm for hydrodynamical interaction of many deformable drops. *J. Comput. Phys.* **157**, 539–587.

Zinchenko, A. Z. & Davis, R. H. 2002 Shear flow of highly concentrated emulsions of deformable drops by numerical simulations. *J. Fluid Mech.* **455**, 21–62.

Zinchenko, A. Z. & Davis, R. H. 2003 Large-scale simulations of concentrated emulsion flows. *Phil. Trans. R. Soc. Lond.* A **361**, 813–845.

Zinchenko, A. Z. & Davis, R. H. 2004 Hydrodynamical interaction of deformable drops. In *Emulsions: Structure Stability and Interactions* (ed. D. N. Petsev), pp. 391–447. Elsevier.

Zinchenko, A. Z. & Davis, R. H. 2005 A multipole-accelerated algorithm for close interaction of slightly deformable drops. *J. Comput. Phys.* **207**, 695–735.

Zinchenko, A. Z., Rother, M. A. & Davis, R. H. 1997 A novel boundary-integral algorithm for viscous interaction of deformable drops. *Phys. Fluids* **9**, 1493–1511.

Zinchenko, A. Z., Rother, M. A. & Davis, R. H. 1999 Cusping, capture and breakup of interacting drops by a curvatureless boundary-integral algorithm. *J. Fluid Mech.* **391**, 249–292.